Heat transfer from a flat plate in inhomogeneous regions of grid-generated turbulence

G. Melina*[1], P. J. K. Bruce[1], J. Nedić[2], S. Tavoularis[3], and J. C. Vassilicos[1]

[1]Department of Aeronautics, Imperial College London, London SW7 2AZ, United Kingdom
[2]Department of Mechanical Engineering, McGill University, Montreal, Quebec H3A 0C3, Canada
[3]Department of Mechanical Engineering, University of Ottawa, Ottawa, Ontario K1N 6N5, Canada

Abstract

Experiments on the convective heat transfer from a flat plate, vertically mounted and parallel to the flow in a wind tunnel, were carried out via Infra-Red thermography and hot-wire anemometry. The Reynolds number based on the inflow velocity and on the length of the plate was about 5×10^5. A step near the leading edge of the plate was used to promote transition to turbulence, with tripping effects on the heat transfer coefficients shown to be negligible for more than 90% of the plate's length. Different types of grids, all with same blockage ratio $\sigma_g = 28\%$, were placed upstream of the plate to investigate their potential to enhance the turbulent heat transfer. These grids were of three classes: regular square-mesh grids (RGs), single-square grids (SSGs) and multi-scale inhomogeneous grids (MIGs). The heat transfer coefficients at the mid-length of the plate were correlated with the mean velocity and the turbulence intensity of the flow at a distance from the plate at which the ratio of the standard deviations of the streamwise and wall-normal velocity fluctuations began to increase. However, the heat transfer was shown to be insensitive to the turbulence intensity of the incoming flow in close proximity of the tripping step. Furthermore, the integral length scale of the streamwise turbulent fluctuations was found not to affect the heat transfer results, both near the tripping step and in the well-developed region on the plate. For the smallest plate-to-grid distance, the strongest heat transfer enhancement (by roughly 30%) with respect to the no-grid case was achieved with one of the SSGs. For the largest plate-to-grid distance, the only grid producing an appreciable increase (by approximately 10%) of the heat transfer was one of the MIGs. The present results demonstrate that MIG design can be optimised to maximise the overall heat transfer from the plate. A MIG that produces a uniform transverse mean shear, which is approximately preserved over significant downstream distances from the grid and with a velocity decreasing with distance from the plate, allows a sustained heat transfer enhancement, in contrast to all other grid designs tested here. The most efficient configuration for a MIG is one for which the section of the grid that has lower blockage and thicker bars is adjacent to the plate.

Keywords: forced convection; flat plate; grid-generated turbulence; IR thermography

*Email address for correspondence: g.melina13@imperial.ac.uk

List of symbols

Greek symbols

β coefficient of thermal expansion of air

ϵ turbulent kinetic energy dissipation rate per unit mass

ε_p emissivity of black paint

δ_{99} 99% boundary layer thickness

η Kolmogorov length scale

Θ_u integral time scale of u

λ Taylor length scale

ν kinematic viscosity

ν_t turbulent viscosity

ρ density

σ_g blockage ratio of the grid

σ_{SB} Stefan-Boltzmann constant, $\sigma_{SB} = 5.67 \times 10^{-8}\,\mathrm{W\,m^{-2}\,K^{-4}}$

τ dimensionless strain

Roman symbols

A_p area of the heated section of the flat plate

c_p specific heat capacity

C_ϵ dissipation coefficient

d_{hw} diameter of the hot-wire

d_p distance between the heated side of the flat plate and the nearest wind tunnel's lateral wall

$\mathcal{D}_i$ measured values of St/St_∞^{NG}

E_{1e} mean value of $\overline{St_\infty}/\overline{St_\infty^{NG}}$ in $0.3 \leq X/L_p \leq 0.4$

E_2 mean value of $\overline{St_\infty}/\overline{St_\infty^{NG}}$ in $0.45 \leq X/L_p \leq 0.85$

$E_{1e,2}$ mean value between E_{1e} and E_2

E_u (E_v) power spectral density of u (v)

f frequency

f_{sh} vortex shedding frequency of the largest bars of the grid

$\mathcal{F}_i$ values of St/St_∞^{NG} predicted by the fit

g gravitational acceleration

Gr_{H_p} Grashof number based on H_p

h convective heat transfer coefficient

H_p height of the flat plate

h_s height of the step (trip) on the flat plate

H_t height of the wind tunnel's test section (or total length of the cylinder)

I electric current

k streamwise wavenumber, $k = 2\pi f/U$

K_p pressure gradient parameter

k_s mean shear rate parameter in the z-direction

L_0 distance between the largest bars of the grid

l_{hw} sensing length of the hot-wire

L_j distance between the bars in the j-th iteration of the multi-scale grids

L_m average value of the distance between the bars of the central iterations of the multi-scale grids

L_p length of the heated section of the flat plate

L_u integral length scale of u in the streamwise direction, $L_u = U\Theta_u$

L_ϵ dissipation length scale

n_j number of bars in the j-th iteration of the MIGs

q_{cond} heat flux lost by thermal conduction

q_{conv} convective heat flux

q_{input} input heat flux

q_{rad} radiative heat flux

R^2 coefficient of determination of the fit

Re_θ boundary layer momentum thickness Reynolds number

Re_{L_0} inlet Reynolds number based on U_∞ and L_0

Re_{t_0} inlet Reynolds number based on U_∞ and t_0

Re_X Reynolds number based on U_∞ and X

Re_{H_p} Reynolds number based on U_∞ and H_p

res sum of squared residuals

St local Stanton number

$\overline{St}$ vertically averaged value of St

T temperature

t_0 thickness of the largest bars of the grid in the $y-z$ plane

T_{aw} adiabatic wall temperature

T_{film} film temperature

t_m average value of the thickness of the bars for the central iterations of the multi-scale grids

t_p thickness (in the $x-z$ plane) of the flat plate

t_w thickness of the Inconel foil covering the flat plate

u, v, w streamwise (along x), vertical (along y), transverse (along z) velocity fluctuations

u', v', w' standard deviations of u, v, w

$\widetilde{U}$, $\widetilde{V}$, $\widetilde{W}$ streamwise (along x), vertical (along y) and transverse (along z) instantaneous velocity components

U, V, W time-averaged values of $\widetilde{U}$, $\widetilde{V}$, $\widetilde{W}$

U_∞ inlet velocity (upstream of the grids)

V_D voltage drop

w_s width of the step (trip) on the flat plate

w_{LE} width of the flat plate's leading edge

W_t width of the wind tunnel's test section

x^* wake interaction length scale for the largest bars of the grids

x_m^* wake interaction length scale for the central iterations of the MIGs

x_{LE} distance between the leading edge of the flat plate and the grid

x_{peak} centreline streamwise location of the maximum turbulence intensity

x_{TE} distance between the trailing edge of the flat plate and the grid

xyz reference frame with its origin fixed at the centre of the grid

XYZ reference frame with its origin fixed at the heated side of the flat plate

z_p z-coordinate of the heated side of the flat plate

z_r z-coordinate where res is minimum

Subscripts

c centreline values ($y = z = 0$)

$film$ evaluated at T_{film}

r values at $y = 0$ and $z = z_r$

w wall values

∞ inlet values or based on inlet conditions

Acronyms

FOV Field Of View

FSG Fractal Square Grid

HW Hot-Wire

IR Infra-Red

MIG Multi-scale Inhomogeneous Grid

NG No Grid

RG Regular Grid

SSG Single Square Grid

1 Introduction

Convective heat transfer from a flat plate is a topic of interest in classical fluid mechanics and in many engineering applications, as different industrial devices make use of flat surfaces to exchange heat with a fluid in motion. A relevant example in the renewable energy industry is the case of high-temperature pressurised-air solar receivers, which are key components in solar power tower plants (Serra et al., 2012; Daguenet-Frick et al., 2013). Considerable effort has been made towards achieving the highest possible heat transfer rate in such devices. Among the suggested solutions, there are two main categories: modifications to the heat transfer surface (e.g., by the addition of roughness or riblets) and modifications to the flow upstream of the flat surface (Colleoni et al., 2013). In many cases, the latter approach could be the only practical one, as it does not require alterations of the entire heated surface, which may be undesirable or too cumbersome to make. The present study is focused upon devising strategies to enhance heat transfer from a flat surface that is contained within a duct (in this case the test section of a wind tunnel). Two strategies appear to be potentially effective in this respect. An obvious one would be to increase the near-wall mean velocity, which can be achieved by diverting fluid from distant regions of the cross-section towards the wall. An important condition for this approach would be to sustain the near-wall velocity increase over sufficient distance along the heated surface to make a significant enhancement of the overall heat removal. A second strategy would be to produce near-wall turbulence with an intensity, length scale and structure that would be most effective in enhancing convective heat transfer. Once more, it is essential that such turbulence would be sustained sufficiently to affect appreciably the overall heat removal. Because local mean velocity and turbulence characteristics are intimately interconnected and also depend strongly on upstream conditions, the design of heat transfer enhancement devices cannot be entirely based on intuitive considerations, but needs extensive empirical input.

Early investigations generated a debate on whether the skin friction and/or the heat transfer coefficient in a turbulent boundary layer with zero pressure gradient are affected by free-stream turbulence. Kestin et al. (1961) did not find significant differences between heat transfer in a laminar free-stream and that in a turbulent free-stream, except in the transition region from a laminar to a turbulent boundary layer on the plate. In contrast, Sugawara et al. (1988) reported a noticeable increase of the heat transfer coefficient with turbulence intensity for the same position on the plate. Other studies confirmed that the skin friction and the convective

heat transfer in a turbulent boundary layer are greatly affected by free-stream turbulence (see e.g. Hancock and Bradshaw, 1983; Blair, 1983; Castro, 1984; Thole and Bogard, 1995; Sharp et al., 2009; Dogan et al., 2016). Some of these studies compared turbulent boundary layers with laminar and turbulent free-stream conditions for the same boundary layer momentum thickness Reynolds number Re_θ. Hancock and Bradshaw (1983) correlated the variation of the skin friction coefficient on a flat plate turbulent boundary layer with a purely empirical parameter based on the turbulence intensity outside of the boundary layer and with the ratio L_ϵ/δ_{99}, where L_ϵ is the dissipation length scale which was obtained from the streamwise decay of turbulent kinetic energy with homogeneous and isotropic assumptions, and δ_{99} is the 99% boundary layer thickness. The skin friction was found to increase with turbulence intensity and to decrease with the ratio L_ϵ/δ_{99} for the same Re_θ. Blair (1983) modified the correlating parameter proposed by Hancock and Bradshaw (1983) to also take into account the effect of Re_θ, which was shown to have an impact for $Re_\theta < 5000$ (McDonald and Kreskovsky, 1974). Additionally, it was also found (Maciejewski and Moffat, 1992; Thole and Bogard, 1995) that the heat transfer coefficient in a turbulent boundary layer is positively correlated with the peak value of u' (u' is the standard deviation of the streamwise velocity fluctuations) in the near wall-region, which increases with free-stream turbulence intensity.

Previous research (see Mazellier and Vassilicos, 2010; Gomes-Fernandes et al., 2012; Laizet et al., 2015; Melina et al., 2017) showed that the design of fractal/multi-scale and regular turbulence-generating grids can be optimised to increase the turbulence intensity, and consequently heat transfer, while keeping the grid's blockage ratio low. The centreline location x_{peak} of the maximum turbulence intensity behind a grid was found to depend on the wake-interaction length scale $x^* = L_0^2/t_0$ (Mazellier and Vassilicos, 2010), while the value of this maximum is proportional to the ratio t_0/L_0 (Gomes-Fernandes et al., 2012), where L_0 is the distance between the largest bars of the grid and t_0 is their thickness. These findings suggest that, for a constant value of t_0/L_0, the centreline turbulence intensity profiles could be collapsed for a variety of grids by normalising x with the geometric parameter x^*, where x is the dimensional distance from the grid. This implies that, for the same x, the turbulence intensity would be higher for grids with larger x^* and the same t_0/L_0 when $x > x_{peak}$ (turbulence decay region). However, it is also important to consider that, for the same x, the mean velocity and the turbulence intensity are also noticeably more inhomogeneous for grids with larger x^* (Hurst and Vassilicos, 2007; Mazellier and Vassilicos, 2010; Valente and Vassilicos, 2014; Melina et al., 2016). The present study aims

at exploiting the above mentioned turbulence intensity scaling laws to improve the heat transfer from a wall for a canonical test case, i.e. a flat plate in a wind tunnel.

The main goal of this work is to test different types of single- and multi-scale turbulence-generating grids and to explore ways of optimising grid design towards maximising the enhancement of heat transfer from a flat plate. Three types of grids were used in these experiments: regular grids (RGs), single-square grids (SSGs) and variants of the multi-scale inhomogeneous grids (MIGs) that were recently introduced by Zheng et al. (2018). The grid's blockage ratio σ_g being a key parameter, it was kept approximately constant for all grids tested in the experiments reported here ($\sigma_g = 25\% - 28\%$). This way it was possible to isolate other effects independently from the effect of σ_g, and a fair comparison between the different geometries of the grids could be carried out. The main questions addressed in this study are the following: (i) whether grids with large values of x^* can be effective in increasing the heat transfer when the flat plate is placed in a region where turbulence intensity is the highest but also where the flow is noticeably inhomogeneous; (ii) whether fractal/multi-scale grids can be used to enhance the heat transfer from a flat plate; (iii) whether, for grids with a large bar thickness, it is more beneficial to place the bars close to the heated surface or farther from it; and (iv) whether the heat transfer results can be correlated with some properties of the flow produced by the grids. As distortion of the boundary layer of the plate by the grid turbulence was expected to be a significant, if not a dominant, factor, and the characterisation of distorted boundary layer structure for different free stream conditions would in itself be a very challenging endeavour, we have not performed any velocity measurements within the boundary layer, but instead made practical comparisons among heat transfer rates from the same plate positioned at the same distance from each of several different grids.

The remainder of this paper is structured as follows: in Section 2, the experimental procedure is described; in Section 3, the flow downstream of the grids is characterised; in Section 4, the heat transfer results are presented; in Section 5, an analysis of the velocity and of the heat transfer results is performed; finally, Section 6 concludes the paper.

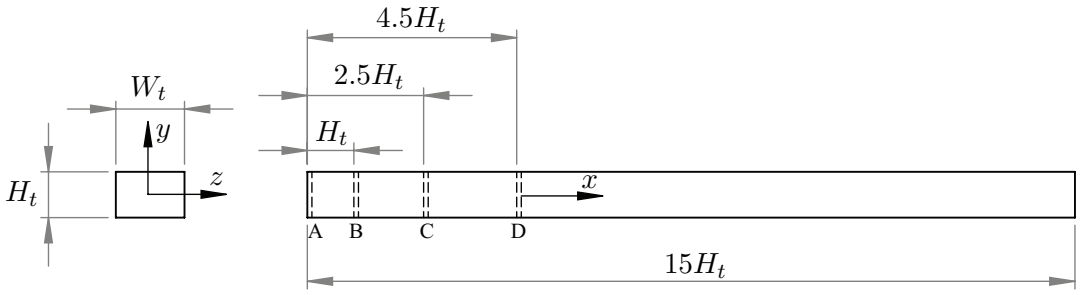

Fig. 1: Sketch of the wind tunnel test section. The letters A to D mark the locations of the four slots where the turbulence-generating grids could be inserted. The origin of the reference frame xyz is fixed at the geometric centre of the grid which, in this drawing, is placed in slot D. The free-stream velocity U_∞ is oriented as the x-axis.

2 Experimental procedure

2.1 The wind tunnel

Experiments were conducted in an open-loop wind tunnel at the University of Ottawa, Canada. The wind tunnel has a 16:1 contraction and a test section with height $H_t = 0.305\,\mathrm{m}$, width $W_t = 1.5H_t$ and working section length of approximately $16.6H_t$. A sketch of the wind tunnel test section is shown in Fig. 1 (see also Fig. 3). Four slots, identified with the letters A to D in Fig. 1, were available for the insertion of different turbulence-generating grids and measurements were performed downstream of them. The origin of the reference system xyz is fixed at the geometrical centre of the grid so that x represents the streamwise distance from the grid whichever slot is used. The inflow velocity U_∞ upstream of the grids was imposed by measuring the static pressure difference across the contraction of the wind tunnel with a digital differential manometer (FCO332, Furness Controls). All measurements were performed with the same inflow velocity, $U_\infty = 8\,\mathrm{m\,s^{-1}}$. The temperature T_∞ of the flow upstream of the grids was measured with a 100 Ω resistance temperature detector (29348-T01-B-48, RDF Corp.).

2.2 Turbulence-generating grids

A total of eleven grids were used to produce turbulent flows in the wind tunnel. Nine grids were specifically designed and manufactured by machining metallic sheets with a thickness of 1.6 mm for the experiments reported in this paper; these grids had the same blockage ratio $\sigma_g = 0.28$ (ratio of the projected area of all grid bars in the $y - z$ plane and $W_t \times H_t$), a value comparable to that of the grids used to enhance heat transfer/scalar diffusion in recent experiments on grid-

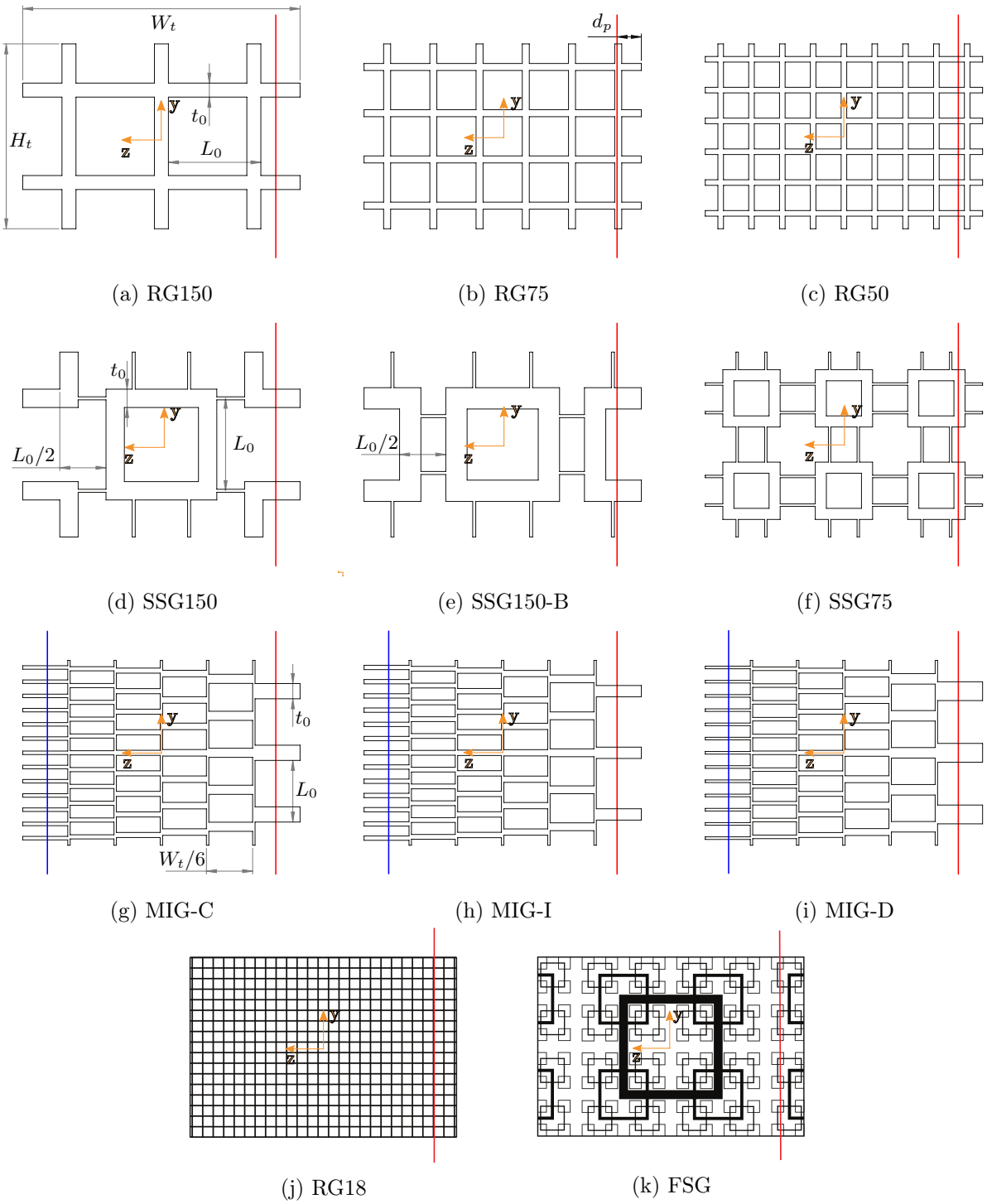

(a) RG150 (b) RG75 (c) RG50

(d) SSG150 (e) SSG150-B (f) SSG75

(g) MIG-C (h) MIG-I (i) MIG-D

(j) RG18 (k) FSG

Fig. 2: Scaled diagrams of the grids used in the experiments. The red vertical lines mark the transverse position of the heated side of the flat plate with respect to the grids. The blue vertical lines in (g), (h) and (i) mark the transverse position of the heated side of the flat plate with respect to the MIGs for the configurations MIG-C$^-$, MIG-I$^-$ and MIG-D$^-$.

generated turbulence (Cafiero et al., 2014; Nedić and Tavoularis, 2016b; Cafiero et al., 2017; Melina et al., 2017). Scaled diagrams of these nine grids are presented in Figs. 2(a)-(i). In this paper, L_0 is the distance between the largest bars (rectangular prisms) of the grids and t_0 is

Grid	RG150	RG75	RG50	SSG150	SSG150-B	SSG75	MIG-C	MIG-I	MIG-D	RG18	FSG
L_0 [mm]	152	76	51	152	152	76	102	102	102	18	163
t_0 [mm]	23	12	8	30	29	18	25	19	31	2	15
x_m^* [mm]	1006	503	335	768	795	317	157	156	154	135	1 739
σ_g	0.28	0.28	0.28	0.28	0.28	0.28	0.28	0.28	0.28	0.25	0.25
Re_{L_0}	80 200	40 100	26 700	80 200	80 200	40 100	53 500	53 500	53 500	9 500	85 600
Re_{t_0}	12 200	6 100	4 100	15 900	15 400	9 600	13 200	9 800	16 300	1 300	8 000

Table 1: Geometric parameters of the grids and inlet Reynolds numbers Re_{L_0} and Re_{t_0} ($U_\infty = 8\,\mathrm{m\,s^{-1}}$).

Grid	MIG-C	MIG-I	MIG-D
$j = 0$	0.25	0.18	0.31
$j = 1$	0.25	0.21	0.28
$j = 2$	0.25	0.24	0.26
$j = 3$	0.25	0.26	0.24
$j = 4$	0.25	0.28	0.21
$j = 5$	0.25	0.31	0.18

Table 2: Values of t_j/L_j for the multi-scale inhomogeneous grids.

their thickness in the $y-z$ plane. The geometric parameters of the grids and the inlet Reynolds numbers Re_{L_0} and Re_{t_0} are reported in Table 1, with $Re_{L_0} = U_\infty L_0/\nu_\infty$, $Re_{t_0} = U_\infty t_0/\nu_\infty$, where ν_∞ is the kinematic viscosity of air evaluated at the temperature T_∞. Among the grids shown in Fig. 2, three grids have a regular square-mesh geometry and are named RG150, RG75 and RG50, where the number in their name identifies the approximate value of their L_0 in mm (see Table 1). Three grids, named SSG150, SSG150-B and SSG75, are obtained by a different arrangement and size of single squares connected with 4 mm thick supporting struts. The last three grids shown in Fig. 2, namely MIG-C, MIG-I and MIG-D, are multi-scale inhomogeneous grids which, unlike the other grids, are not symmetric with respect to the y-axis. Two additional grids were also used for some of the measurements reported in this paper. These are a regular grid, RG18 (Fig. 2(j)), with a very small L_0, and a multi-scale fractal square grid, FSG (Fig. 2(k)), with four geometric iterations and a value of L_0 comparable to that of SSG150 and SSG150-B. The grids RG18 and FSG had a blockage ratio of $\sigma_g = 0.25$, which is slightly lower than the value 0.28 of the other nine grids; these two grids were recently used in the turbulent diffusion study by Nedić and Tavoularis (2016b).

The multi-scale inhomogeneous grids (MIGs) were designed following the work of Zheng et al. (2018) and are formed by six layers ($j = 0, \ldots, 5$) of bars with separation L_j and thickness t_j, where $j = 0$ identifies the layer (iteration) with the largest L_j. Every layer has the same width, $W_t/6$, and the number of bars n_j varies across the layers according to $n_{j+1} = n_j + 2$ ($j = 0, \ldots 4$), n_0=3. The distance between the bars in each layer is $L_j = H_t/n_j$ ($j = 0, \ldots 5$). The MIGs were designed by varying the ratios t_j/L_j, *i.e.* by varying the blockage ratio across the layers, with the purpose of producing a flow with a moderate mean shear rate $\partial U/\partial z$, where U is the streamwise

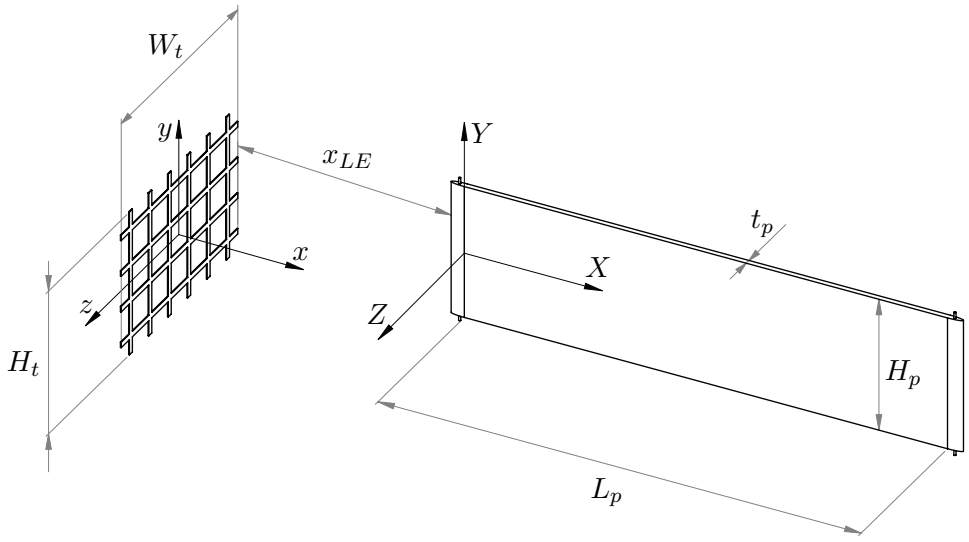

Fig. 3: Schematic arrangement of the flat plate with respect to a representative turbulence-generating grid.

component of the mean velocity. The values of t_j/L_j for the three MIGs are reported in Table 2. The ratio t_j/L_j is constant with j for MIG-C ("C" stands for constant), increases with j for MIG-I ("I" stands for increasing) and decreases with j for MIG-D ("D" stands for decreasing). A number of measurements were also performed with the MIGs in the opposite orientation to that shown in Figs. 2(g)-(i) by rotating these grids by 180° around y. The configurations with the grids MIG-C, MIG-I and MIG-D in the opposite orientation are identified in this article by MIG-C$^-$, MIG-I$^-$ and MIG-D$^-$, respectively.

2.3 Flat plate

A flat plate was vertically placed in the wind tunnel's test section downstream of the turbulence-generating grids. A sketch of the grid-plate arrangement is shown in Fig. 3. For most of the measurements, the distance between the leading edge (LE) of the plate and the grid was $x_{LE}/H_t = 1.5$ (grid inserted in slot D). Some measurements were also performed with the plate farther downstream with respect to the grids, so that $x_{LE}/H_t = 5$ (grid inserted in slot B). The leading edge and the trailing edge of the plate were made of copper and had an elliptical section. They were mechanically pressed to a Polyoxymethylene (POM) substrate with height $H_p = 0.28\,\mathrm{m}$, length $L_p = 1\,\mathrm{m}$ and thickness $t_p = 11\,\mathrm{mm}$ (see Fig. 3). A metallic foil made of Inconel 600 and with nominal thickness $t_w = 12.5\,\mu\mathrm{m}$ was tight-fitted between the two copper pieces and the POM substrate. The foil entirely covered one side of the plate, electrically connecting

leading and trailing edges. This is the side of the plate where the heat transfer measurements were performed and is henceforth referred to as the heated side. A double-sided adhesive (with thermal conductivity of $0.08\,\mathrm{Wm^{-1}K^{-1}}$) ensured a flat contact between the Inconel foil and the plastic substrate. The distance d_p (see Fig. 2(b)) between the heated side and the nearest lateral wall of the wind tunnel was 40 mm for all measurements performed with the plate in the wind tunnel. The value of d_p was imposed by the experimental set-up, i.e. it was the minimum distance which allowed the placement of the plate together with its supports, power cables and sensor cables in the test section. In order to promote the development of a turbulent boundary layer on the heated side, the leading edge included a step with height $h_s = 1\,\mathrm{mm}$ and width $w_s = 1.5\,\mathrm{mm}$, placed at a distance of 30 mm from the leading edge. A second reference system XYZ is defined with its origin fixed at the wall of the plate (see Fig. 3), with $X = x - (x_{LE} + w_{LE} + w_s)$, $Y = y$ and $Z = z + W_t/2 - d_p$, where w_{LE} is the width of the leading edge ($w_{LE} = 30\,\mathrm{mm}$).

2.4 Velocity measurements

Velocity measurements downstream of the grids were performed with two-component hot-wire (HW) anemometry using a cross-wire (XW) probe which was operated by a constant temperature anemometer (AN-1003, A.A. Lab Systems). The XW probe had two sensing tungsten wires with diameter $d_{hw} = 2.5\,\mu\mathrm{m}$ and length $l_{hw} \approx 0.8\,\mathrm{mm}$, with the separation between the two wires being approximately 0.5 mm. The HW measurements were performed both with and without the flat plate in the wind tunnel. For each measurement point, the HW voltage signal was acquired at a sampling frequency of 35 kHz with the analogue low-pass filter set at 14 kHz and with a sampling time of 150 s, which corresponds to at least 18 000 integral time scales for the largest integral time scale. Data were recorded using a 16-bit data acquisition system (NI-6143, National Instruments).

Measurements along the centreline ($y = z = 0$) were performed by traversing the XW probe in the streamwise direction x in order to measure the instantaneous velocity components $\widetilde{U}$ (in the x-direction) and $\widetilde{V}$ (in the y-direction). In this case, the probe was calibrated *in situ* by rotating it in the $x - y$ plane for different velocities U_∞, following the "look-up table" calibration procedure described in Lueptow et al. (2004). During the calibrations, the velocity U_∞ was controlled with the use of a Pitot tube located in the proximity of the XW probe and connected to the digital manometer. Measurements of the velocity profiles along the direction z were performed at a series of streamwise stations for $y = 0$. In this case the HW calibrations were

performed by rotating the XW probe in the $x-z$ plane in order to measure the instantaneous velocity components $\widetilde{U}$ and $\widetilde{W}$ (in the z-direction).

The velocity fluctuations u, v and w were obtained by subtracting the time-averaged velocities U, V and W from $\widetilde{U}$, $\widetilde{V}$ and $\widetilde{W}$ respectively. The standard deviations of u, v and w are denoted u', v' and w', respectively. The integral time scale of u was calculated as (Pope, 2000):

$$\Theta_u = \frac{E_u(f=0)}{4u'^2}, \tag{1}$$

where $E_u(f)$ is the power spectral density of u in the frequency domain f. In particular $E_u(f=0)$ was estimated by averaging $E_u(f)$ in the low-frequency range, where $E_u(f)$ remained approximately constant for at least one decade of frequencies for the grids that produced the largest values of Θ_u. The integral length scale L_u of u in the x-direction was computed assuming Taylor's frozen flow approximation, $L_u = U\Theta_u$, as in other experimental studies on grid-generated turbulent flows (see, for example, Hurst and Vassilicos, 2007; Sak et al., 2007; Mazellier and Vassilicos, 2010; Nagata et al., 2013; Nedić and Tavoularis, 2016b). The turbulent kinetic energy dissipation rate ϵ was computed from its isotropic definition:

$$\epsilon = 15\nu_\infty \left\langle \left(\frac{\partial u}{\partial x}\right)^2 \right\rangle , \tag{2}$$

where

$$\left\langle \left(\frac{\partial u}{\partial x}\right)^2 \right\rangle = \int_0^{k_{max}} k^2 E_u(k)\,\mathrm{d}k \tag{3}$$

and $\langle\cdot\rangle$ denotes the time-averaging operator. The conversion from frequencies f to wavenumbers k was obtained with Taylor's approximation as $k = 2\pi f/U$, $E_u(k) = UE_u(f)/(2\pi)$. The value of k_{max} in Eq. 3 was determined by the cut-off frequency of the analogue low-pass filter of the anemometer. The frequency response of the hot-wire used for the present measurements was high enough to resolve the dissipation spectrum $k^2E_u(k)$ up to at least $k = 1/\eta$, where $\eta = \left(\nu_\infty^3/\epsilon\right)^{1/4}$ is the Kolmogorov microscale. The spatial resolution l_{hw}/η ranged approximately from 2 to 7. The Taylor microscale λ was computed as $\lambda = \left(15\nu_\infty u'^2/\epsilon\right)^{1/2}$.

2.5 Heat transfer measurements

Heat transfer measurements were performed on the side of the plate that was covered with the Inconel foil. A DC laboratory power supply was connected across the leading and trailing edges

of the plate (copper terminals) so that the foil was heated by Joule effect, thus approximating a uniform heat flux wall boundary condition. The Inconel foil was painted with black paint (1602, Krylon), which has a known emissivity $\varepsilon_p = 0.95$, and the wall temperature T_w was measured with an infrared (IR) camera (A325sc, FLIR). The IR camera was placed outside of the wind tunnel and it was focused on the heated side of the plate through circular windows on the lateral wall of the test section. For all the grids tested here, the camera was focused on the upstream half of the plate ($0.03 \leq X/L_p \leq 0.4$), which is referred to as FOV1 (Field Of View 1). For some configurations, measurements were also performed on the downstream half of the plate ($0.45 \leq X/L_p \leq 0.85$) named FOV2. The spatial resolution of the temperature measurements on the plate was $\Delta X = \Delta Y \approx 1.3\,\mathrm{mm}$.

The following procedure was systematically used for the temperature measurements on the flat plate. The wind tunnel was turned on and a settling time was allowed in order for the temperature of the flow T_∞ to become stable at the desired velocity U_∞. Two-dimensional instantaneous maps of the adiabatic wall temperature distribution (temperature distribution on the foil without Joule heating), which are referred to as "*cold images*", were acquired at this point using the IR camera. The electric power was then delivered to the foil with the power supply set in constant current mode. Finally, instantaneous maps of heated foil temperature, which are referred to as "*hot images*", were acquired with the IR camera after allowing enough time (approximately 45 minutes) for steady state conditions to be reached. The time-averaged values of the adiabatic wall temperature, T_{aw}, and those of the heated wall temperature, T_w, were obtained by averaging 900 frames acquired with the camera at a sampling frequency of 60 Hz. Note that in this experiment the temperature T_{aw} was almost coincident with T_∞. In order to take into account possible variations of T_{aw} between the acquisition of the cold images and that of the hot images, the values of T_{aw} were corrected with the difference between the value of T_∞ measured together with the hot images and that measured with the cold images (see Cafiero et al., 2017). Note that this correction was very small, because the temperature of the laboratory during each experiment was kept stable within 0.2 K. The acquisition of the raw images (measurement signal) and their conversion to IR images (temperature signal) were performed by using the IR camera's software (FLIR ResearchIR Max®) and the calibration curves provided by the camera's manufacturer.

The convective heat transfer coefficient h was computed as

$$h = \frac{q_{conv}}{T_w - T_{aw}}, \tag{4}$$

where q_{conv} is the convective heat flux, which was calculated from the energy balance at the wall as

$$q_{conv} = q_{input} - q_{rad} - q_{cond}. \tag{5}$$

In this expression the input heat flux is $q_{input} = V_D I / A_p$, where V_D is the voltage drop across the length of the foil, I is the electric current and the area of the heated foil is $A_p = L_p H_p$. The voltage V_D was measured with the data acquisition system by connecting two electric cables to the leading and trailing edges of the plate (copper terminals). The current I was calculated by measuring the voltage drop across a precision shunt resistor of known electrical resistance, which was connected in series with the Inconel foil and the power supply. For almost all experiments, the current provided to the foil was kept constant at approximately $I = 30\,\mathrm{A}$, thus making a comparison possible between the different configurations (grids) with the same input heat flux. The term q_{rad} in Eq. 5 is the radiative heat flux, which was computed as

$$q_{rad} = \varepsilon_p \sigma_{SB} (T_w^4 - T_\infty^4), \tag{6}$$

where σ_{SB} is the Stefan-Boltzmann constant. The value of the ratio q_{rad}/q_{input} was about 15% for typical values of T_w and T_∞ in this experiment. The heat flux q_{cond} lost by conduction through the plate's core was estimated using Fourier's law by measuring the temperature at a series of positions on the unheated side with a K-type thermocouple. The heat flux q_{cond} accounted for about 9% of the input heat flux q_{input}. Preliminary heat transfer measurements (without grids in the wind tunnel) were performed for the same U_∞ with three different values of input current I (and so different ranges of $T_w - T_{aw}$) to verify that applying the correction for thermal conduction produced consistent and repeatable results. These measurements (reported in Section 4.2) revealed that the Stanton number (non-dimensional heat transfer coefficient defined in Eq. 8) changed less than 1% among the three sets of measurements, thus validating the experimental technique and the data reduction process followed here. Table 3 reports typical values and associated measurement uncertainties for each quantity used to compute h. A single-sample uncertainty analysis using a 95% confidence interval was carried out following Moffat (1988).

Quantity	Typical value	Uncertainty
L_p	1000 mm	1 mm
H_p	280 mm	1 mm
V_D	9.0 V	$0.01 \times V_D$
I	30.1 A	$0.01 \times I$
T_∞	296 K	0.1 K
T_w	319 K	0.2 K
T_{aw}	296 K	0.2 K
ε_p	0.95	0.01
h	$34\,\mathrm{Wm^{-2}K^{-1}}$	4.4%

Table 3: Typical values and associated measurement accuracies for the different quantities used to compute h, and typical relative measurement uncertainty (estimated using a 95% confidence interval) for h.

The typical resulting total uncertainty of the computed values of h is 4.4%. Considering typical values of T_w and T_∞ (see Table 3), the Grashof number, based on the height H_p of the flat plate, is $Gr_{H_p} = g\beta\,(T_w - T_\infty)\,H_p^3/\nu_{film}^2 = 5.9 \times 10^7$ (g is the gravitational acceleration and $\beta = 1/T_{film}$ is the coefficient of thermal expansion of air). The resulting Richardson number $Gr_{H_p}/Re_{H_p}^2$ is about 0.003, with $Re_{H_p} = U_\infty H_p/\nu_{film} = 1.4 \times 10^5$. Since $Gr_{H_p}/Re_{H_p}^2 << 1$, the effects of natural convection are expected to be negligible with respect to those due to forced convection (Hewitt, 2008).

3 Mean and turbulent velocity fields produced by the grids

The flow past the nine grids shown in Fig. 2 was characterised without the flat plate in the wind tunnel. For this purpose, HW velocity measurements were first performed along the centreline ($y = z = 0$) in order to obtain the streamwise evolution of the main turbulence statistics, with particular focus on turbulence intensity. Secondly, velocity measurements were carried out at a series of stations along the direction normal to the plate ($z-$axis) downstream of the three MIGs in order to document the mean shear produced by each grid and the corresponding profiles of turbulence statistics.

3.1 Measurements along the wind tunnel centreline

The centreline turbulence intensity u_c'/U_∞ downstream of the three categories of grids (RGs, SSGs and MIGs) is shown in Fig. 4(a), whereas additional centreline turbulence statistics are reported in the Appendix. For the grids RG75, SSG150 and SSG150-B, it is possible to identify a streamwise location x_{peak}, where u_c'/U_∞ was maximum. This location was $x_{peak} = 1.02H_t$ for

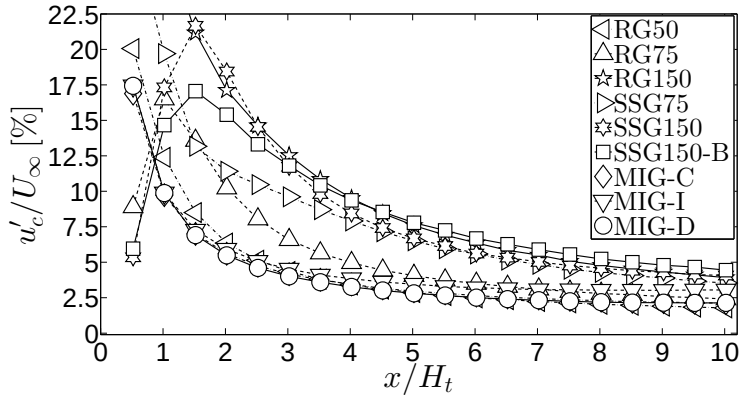

(a)

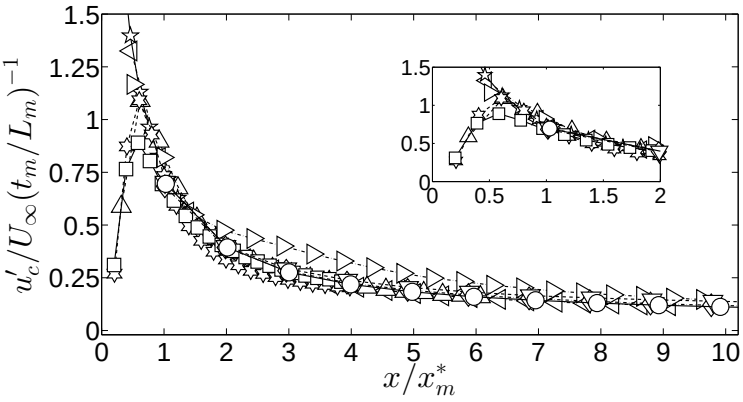

(b)

Fig. 4: Centreline turbulence intensity for RGs, SSGs and MIGs.

RG75 and $1.52H_t$ for both SSG150 and SSG150-B. When normalised by the wake-interaction length scale $x^* = L_0^2/t_0$, which characterises the location at which the wakes of the bars of the grid meet on the centreline, the location of the peaks was nearly the same for these three grids ($x_{peak}/x^* = 0.62, 0.60$ and 0.58 for RG75, SSG150 and SSG150-B, respectively). Considering that all grids shown in Fig. 2 had the same blockage ratio ($\sigma_g = 0.28$), the previous finding is consistent with the literature (Mazellier and Vassilicos, 2010; Laizet and Vassilicos, 2011; Gomes-Fernandes et al., 2012; Laizet et al., 2015; Nedić and Tavoularis, 2016b; Melina et al., 2016).

The peak value of u_c'/U_∞ behind fractal square grids has been found to be proportional to the ratio t_0/L_0 (Gomes-Fernandes et al., 2012). For the RGs and SSGs, the lengths L_0 and t_0 apply to all elements, including those near the centreline, but this is not the case for the MIGs. Scales that are more representative for the near-centreline elements of such grids can be defined as $L_m = (L_3 + L_4)/2$ and $t_m = (t_3 + t_4)/2$, which are, respectively, the average distance between the bars and the average thickness amongst the layers $j = 3$ and $j = 4$ in the

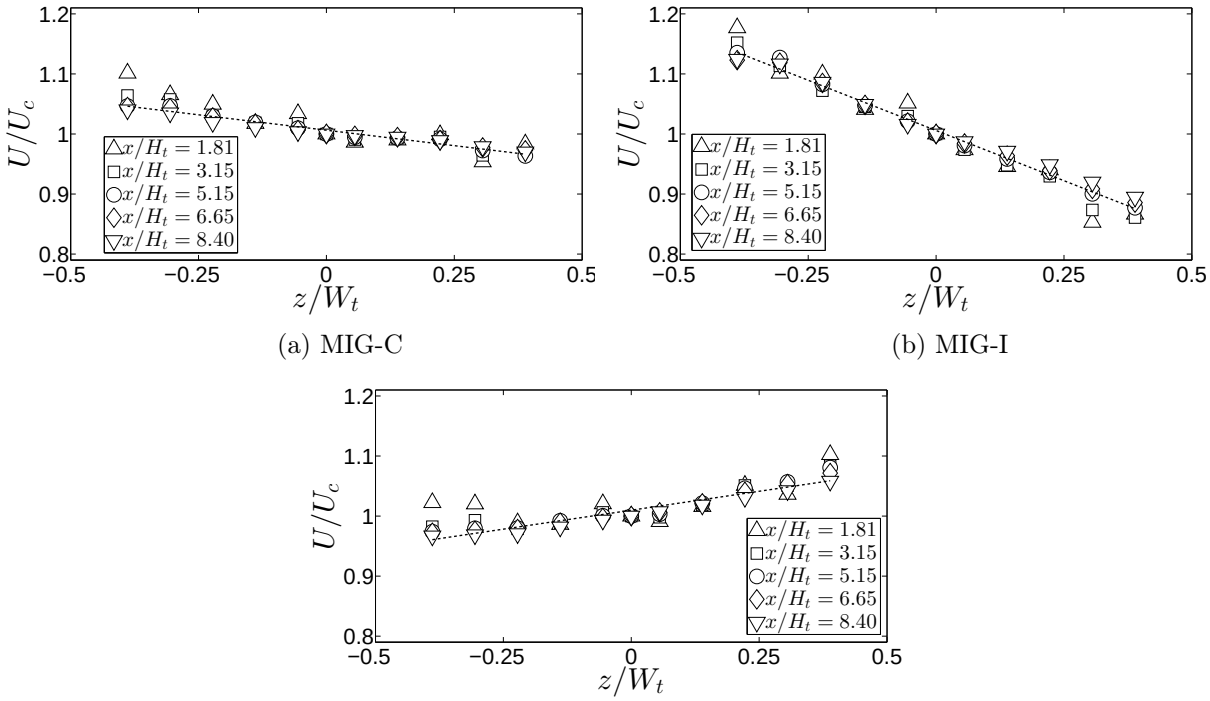

(a) MIG-C

(b) MIG-I

(c) MIG-D

Fig. 5: Transverse profiles of U/U_c for MIG-C (a), MIG-I (b) and MIG-D (c). The dashed lines in are linear fits of the mean velocity profiles.

grid (Fig. 2(g)-(i)). For the RGs and SSGs one can consider that $L_m = L_0$ and $t_m = t_0$. A universal centreline wake-interaction length can then be defined as $x_m^* = L_m^2/t_m$. The values of this parameter for the different grids are reported in Table 1. Fig. 4(b) shows that values of the ratio $(u_c'/U_\infty)/(t_m/L_m)$ behind different grids essentially collapsed on each other when plotted against x/x_m^*. This demonstrates that geometrical features of the grid are sufficient for the prediction of both the centreline location of the maximum of turbulence intensity and its magnitude, and that this observation applies not only to regular and fractal square grids, but also to MIG-type grids.

3.2 Measurements in a direction normal to the plate

Velocity profiles along the z-direction were taken downstream of the MIGs at five streamwise stations for $-0.4 \leq z/W_t \leq 0.4$ and for $1.8 \leq x/H_t \leq 8.4$ ($y = 0$), with the grids oriented as in Figs. 2(g)-(i). The mean velocity profiles, normalised with the centreline values U_c, are presented in Figs. 5(a)-(c). These results show that the variation of the ratio t_j/L_j across the layers of the MIGs (see Table 2) produced different profiles of U/U_c for MIG-C, MIG-I and MIG-D. In particular, $\partial U/\partial z$ was negative for MIG-C and MIG-I and positive for MIG-D, with $|\partial U/\partial z|$

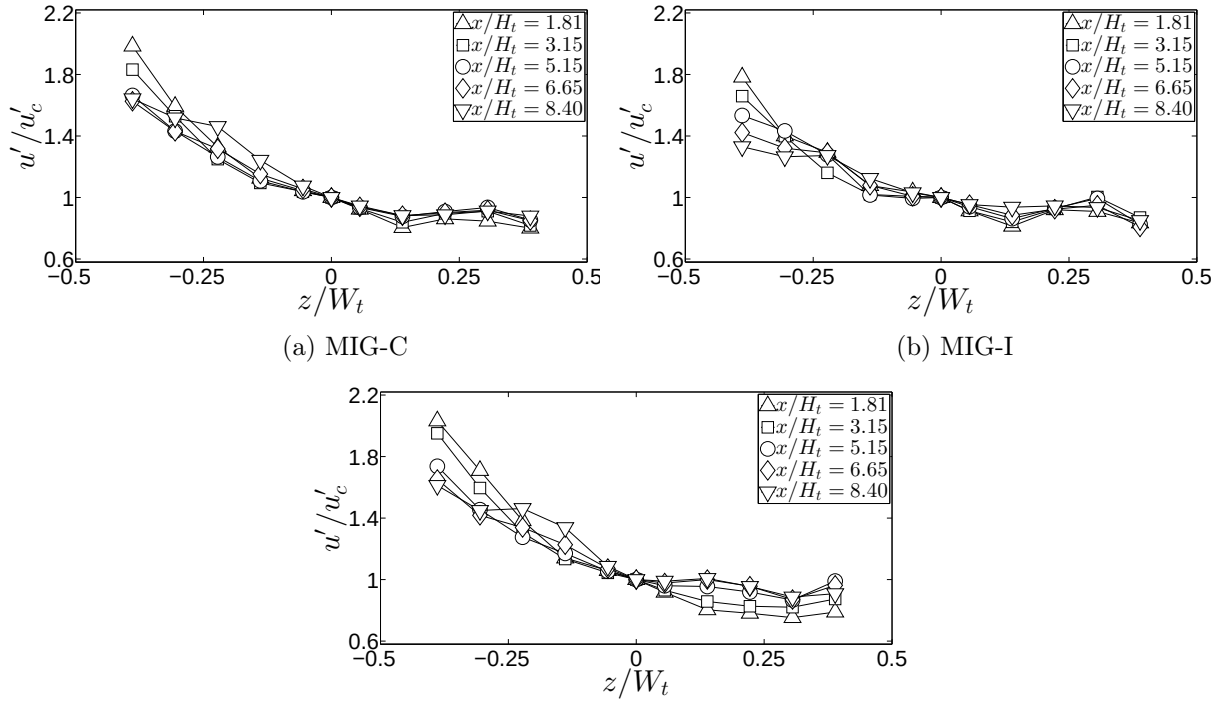

(a) MIG-C (b) MIG-I

(c) MIG-D

Fig. 6: Transverse profiles of u'/u'_c for MIG-C (a), MIG-I (b) and MIG-D (c).

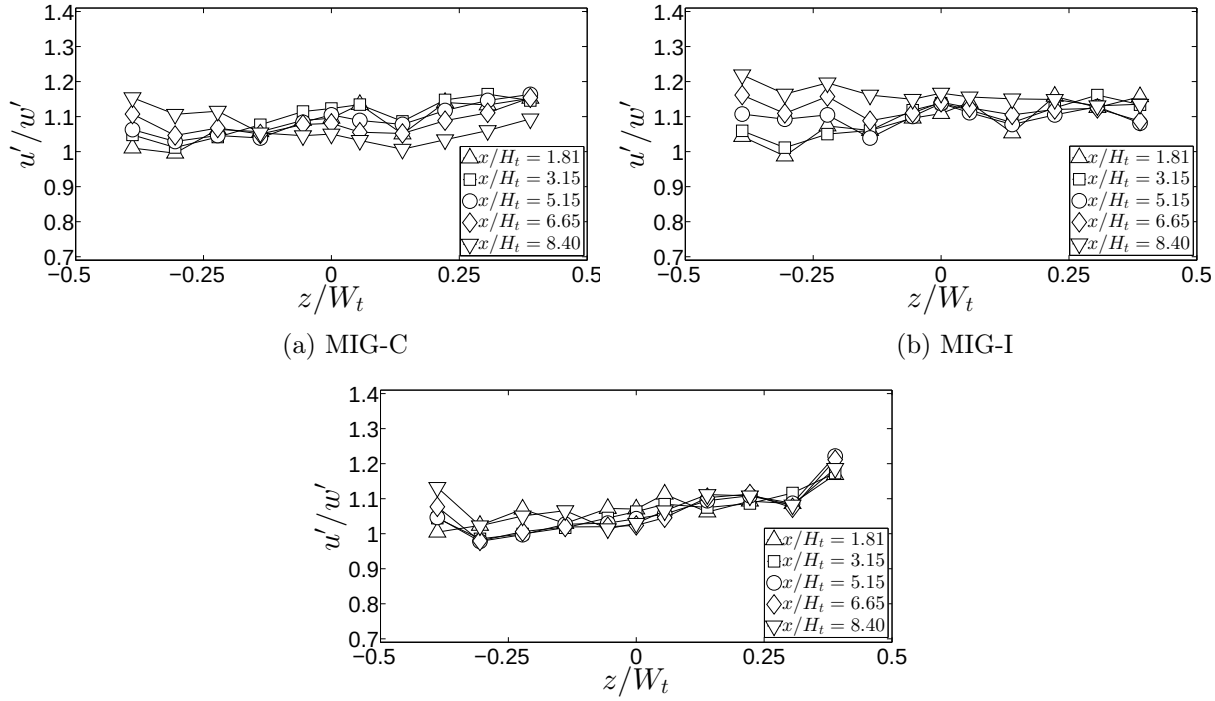

(a) MIG-C (b) MIG-I

(c) MIG-D

Fig. 7: Transverse profiles of u'/w' for MIG-C (a), MIG-I (b) and MIG-D (c).

being the highest for MIG-I. The normalised mean velocity profiles measured at different x were roughly linear and nearly collapsed for $x/H_t \geq 3.15$, thus showing that the shear rate remained

approximately constant with downstream distance from each MIG, at least for the $x-$range tested here. In order to quantify the shear rate for each of the MIGs, the profiles of U/U_c were averaged over x in the range $3.15 \leq x/H_t \leq 8.40$ and a linear fit was applied to the data. The computed shear rate parameter $k_s = U_c^{-1}\partial U/\partial z$ was $-0.22\,\mathrm{m}^{-1}$ for MIG-C, $-0.73\,\mathrm{m}^{-1}$ for MIG-I and $0.28\,\mathrm{m}^{-1}$ for MIG-D. All these values are an order of magnitude smaller than those in previous realisations of uniformly sheared turbulence (k_s was $3.8\,\mathrm{m}^{-1}$ in the experiments of Tavoularis and Corrsin (1981), $5.0\,\mathrm{m}^{-1}$ in those by Rohr et al. (1988) and $6.1\,\mathrm{m}^{-1}$ in the ones by Nedić and Tavoularis (2016a)).

The observed approximate streamwise invariance of the mean velocity profiles ($\partial U/\partial x \approx 0$) downstream of the MIGs can be explained by considering that the streamwise mean momentum equation for a flow which is homogeneous in the vertical direction ($\partial(\cdot)/\partial y \approx 0$), two-dimensional on the mean ($W \approx 0$) and has a uniform mean pressure, is reduced to:

$$U\frac{\partial U}{\partial x} \approx -\frac{\partial < u^2 >}{\partial x} + \nu\frac{\partial^2 U}{\partial x^2} + (\nu + \nu_t)\,\frac{\partial^2 U}{\partial z^2}\ , \tag{7}$$

where the Reynolds stresses $< uw >$ have been expressed as $< uw >= -\nu_t\,\partial U/\partial z$, with ν_t being a turbulent viscosity. Further considering that the magnitude of $\partial < u^2 > /\partial x$ is small for $x/H_t \geq 3.15$ (Fig. 4(a)), and that the streamwise viscous term would also be very small for the present, relatively large, Reynolds number flows, one can conclude that, if the mean velocity transverse profile is approximately linear ($\partial^2 U/\partial z^2 \approx 0$), then $\mid \partial U/\partial x \mid$ would be small as well.

The transverse profiles of u'/u'_c for the MIGs are shown in Figs. 6(d)-(f). Unlike the mean velocity profiles, the profiles of u'/u'_c behind the three MIGS were very similar. For a fixed x, u'/u'_c was highest behind the part of the grid with the widest spacings of the bars (large negative z values), it decreased with decreasing z up to roughly the centreline ($z = 0$) and then remained approximately constant on the side of the grid with the smaller spacings of the bars ($z > 0$). For $z < 0$, u'/u'_c decreased with increasing x, showing a slow tendency for the turbulence to become less inhomogeneous along z. The large-scale anisotropy of the flow downstream of the MIGs remained mild, as evidenced in Figs. 7(g)-(i), which show that the ratio u'/w' remained between 1 and 1.2 throughout the considered range of measurements. Such values are much lower than values of this ratio in previous realisations of uniformly sheared turbulence and show that the structure of the turbulence behind the present MIGs was not shear-dominated. This does not come as a surprise, as the largest value of the dimensionless strain imposed on these flows (the

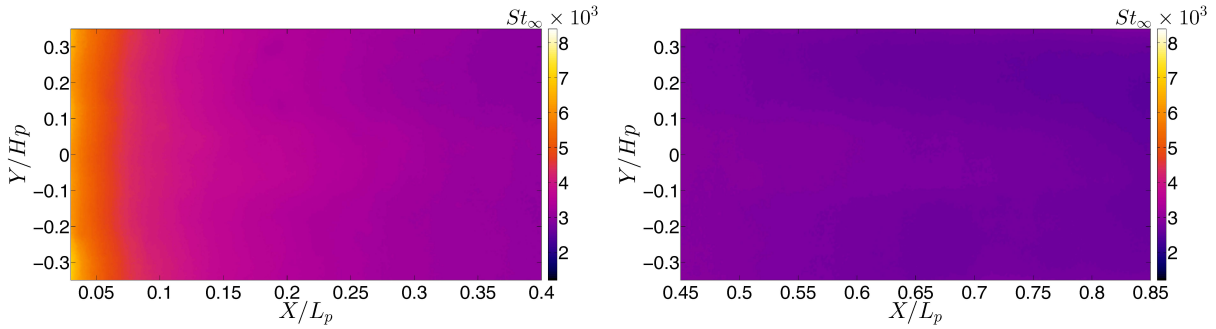

(a) FOV1 (b) FOV2

Fig. 8: Contour plots of St_∞ on the plate without grids ($I \approx 30\,\mathrm{A}$).

one behind MIG-I, at $x/H_t = 8.4$) was $\tau = k_s x \approx 1.9$, which is significantly smaller than the value 5 that is required by uniformly sheared turbulence to reach an asymptotic, self-similar, shear-dominated structure (Tavoularis and Karnik, 1989). In summary, the MIGs used in these experiments produced roughly uniform mean shear with a moderate strength and relatively weak, inhomogeneous and mildly anisotropic turbulence.

4 Heat transfer from the plate

4.1 The mean pressure field

The flat plate was installed vertically in the test section with its leading edge at a distance $x_{LE} = 1.5H_t$ from slot D and with its heated side at a distance $d_p = 0.09W_t$ from the nearest side wall of the wind tunnel (see Fig. 1 and Fig. 3). Before performing the heat transfer measurements, the orientations of both side walls of the wind tunnel were adjusted in an effort to keep the pressure along the plate as uniform as possible. It was found that the mean velocity along the wind tunnel centreline in the presence of the plate, but without any grids, increased approximately linearly by 2% between stations corresponding to the leading and trailing edges. The resulting favourable pressure gradient along the plate had a parameter $K_p = (\nu_\infty/U_\infty^2)(\partial U_c/\partial x) \approx 4.9\times10^{-8}$, which is two orders of magnitude smaller than the threshold 1.6×10^{-6} above which a favourable pressure gradient would cause considerable deviations from the logarithmic law (DeGraaff and Eaton, 2000). Consequently, we can be confident that heat transfer from the present plate would not be affected by the weak pressure gradient. The grid-free centreline turbulence intensity u_c'/U_∞ remained approximately constant along the plate at about 0.2%.

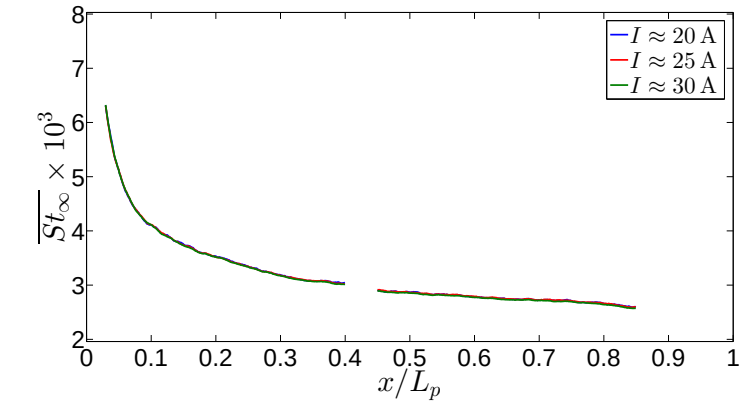

(a)

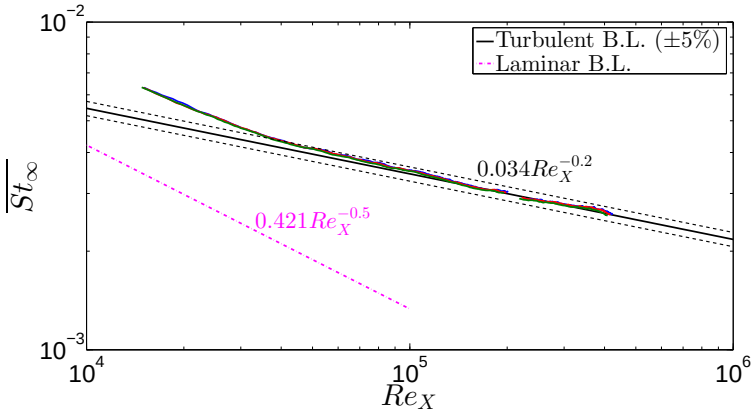

(b)

Fig. 9: Evolution of $\overline{St_\infty}$ along the plate without grids for three heating currents. The black dashed lines in (b) identify a ±5% interval around the correlation for turbulent boundary layers (von Kármán, 1939). $Re_X = U_\infty X/\nu_{film}$, where ν_{film} is the kinematic viscosity of air, evaluated at the film temperature.

4.2 Heat transfer without grids

Heat transfer measurements on the plate were first performed without grids in the wind tunnel in order to validate the experimental technique and to have a baseline case for reference. This configuration is henceforth referred to as the "NG" (No Grid) case. IR temperature measurements were carried out on two sections of the plate (FOV1 and FOV2) following the procedure described in Section 2.5 for three heating currents, $I \approx 20$, 25 and 30 A. The convective heat transfer from the plate was quantified by the Stanton number based on the inlet velocity, which is defined as

$$St_\infty = \frac{h}{\rho_{film} c_{p_{film}} U_\infty}. \tag{8}$$

In this expression, ρ_{film} and $c_{p_{film}}$ are, respectively, the density and the specific heat capacity of air evaluated at the film temperature $T_{film} = (T_w + T_\infty)/2$. Contour plots of St_∞ for the

NG case are shown in Fig. 8. The values of St_∞ were the highest near the leading edge and gradually decreased along X as a result of the thickening of the boundary layer along the plate. St_∞ was essentially uniform along the span of the plate ($Y-$ direction). As shown in Fig. 9(a), the values of the transverse-averaged Stanton number $\overline{St_\infty}$ in the central portion of the plate ($-0.2 \leq Y/H_p \leq 0.2$) for the three heating conditions were indistinguishable from each other. This allows us to consider one heating condition as representative of the others. The same parameter has been plotted in logarithmic axes in Fig. 9(b), together with classical correlations for laminar (Pohlhausen, 1921) and turbulent (von Kármán, 1939; Junkhan and Serovy, 1967) boundary layers. One may identify an initial development region just downstream of the step ($Re_X \lesssim 4 \times 10^4$), where the Stanton number was larger than predictions of either the laminar ($\overline{St_\infty} = 0.421 Re_X^{-0.5}$) or the turbulent ($\overline{St_\infty} = 0.034 Re_X^{-0.2}$) correlation. This discrepancy may be partially attributed to the tripping device (step) used to promote transition and is analogous to a similar discrepancy in the skin friction coefficient on a flat plate with tripping (see, *e.g.*, Erm and Joubert, 1991; Schlatter and Örlü, 2012). An additional cause of this discrepancy could be the fact that the plate was unheated between its leading edge and the location of the trip, which was 30 mm downstream. In the remainder of the plate, however, which corresponded to 92% of its length, the Stanton number remained within 5% of the turbulent prediction. Note that, since it is widely known that a turbulent free-stream promotes transition to turbulence on a flat plate, one can reasonably expect that for the case of heat transfer with grids, tripping effects will be negligible for more than 90% of the plate's length. Note however that hot-wire measurements were also performed in the close proximity ($X/L_p = 0.03$) of the tripping step, with the purpose of studying the effect of turbulence on this "disturbed" area of the plate (see Section 5).

4.3 Selection of the best performing grids

Heat transfer measurements were first performed on the upstream half of the plate (FOV1) with all turbulence-generating grids placed in slot D ($x_{LE}/H_t = 1.5$). The purpose of these measurements was to identify the "best performing" configurations, *i.e.* the grids that could lead to a substantial heat transfer enhancement with respect to the NG case. As a selection criterion, we used the value of the ratio $\overline{St_\infty}/\overline{St_\infty^{NG}}$, where $\overline{St_\infty}$ is the spatial average of St_∞ in the range $-0.2 \leq Y/H_p \leq 0.2$ and $\overline{St_\infty^{NG}}$ is the value of $\overline{St_\infty}$ for the NG case (shown in Fig. 9) with the same U_∞ and the same input electric power. Fig. 10 shows the obtained $\overline{St_\infty}/\overline{St_\infty^{NG}}$ for all configurations. With the exception of the smallest grid (RG18) case (for which the measurements

Grid	E_{1e}	Grid	E_{1e}	Grid	E_{1e}
RG150	1.03	SSG150	1.28	MIG-C	1.11
RG75	1.12	SSG150-B	0.95	MIG-I	1.20
RG50	1.07	SSG75	0.96	MIG-D	1.06
RG18	0.97	FSG	1.15	MIG-C$^-$	1.03
				MIG-I$^-$	0.93
				MIG-D$^-$	1.13

Table 4: Heat transfer enhancement parameter E_{1e} for all grids; $x_{LE}/H_t = 1.5$.

dis not extend sufficiently close), all cases exhibit an initial region where the growth rate of this ratio is significant and which is followed by a region of much slower growth. This means that at the start of the plate the values of $\overline{St_\infty}$ decreased more slowly in the presence of a grid than for the NG case and further downstream the same decay rate was approximately reached for all cases. As seen in Section 4.2, the portion of the plate in the proximity of the step ($X = 0$) was a transition region which was subject to the effects of the tripping device and where, for the NG case, $\overline{St_\infty}$ decayed faster than for a fully developed turbulent state.

As an overall indicator of the effectiveness of each grid in enhancing heat transfer from the plate, we introduce the enhancement parameter E_{1e}, defined as the average value of $\overline{St_\infty}/\overline{St_\infty^{NG}}$ in a representative downstream slow-evolution region ($0.3 \leq X/L_p \leq 0.4$) in FOV1. The values of this enhancement parameter for all grids are listed in Table 4. This table, together with Fig. 10, show that the grids can be divided in two categories: a) those that did not significantly alter the heat transfer with respect to the NG case ($0.93 \leq E_{1e} \leq 1.07$); these included grid of all three types (RG150, RG50, RG18, SSG150-B, SSG75, MIG-D, MIG-C$^-$ and MIG-I$^-$); and b) those that enhanced the overall heat transfer by more than 10%; these also included grids of all three types (RG75, SSG150, FSG, MIG-C, MIG-I and MIG-D$^-$). The strongest heat transfer enhancement ($E_{1e} = 1.28$) among all grids was produced by SSG150. This is contrasted sharply by the effect of SSG150-B, which although bares a geometrical resemblance with SSG150, actually produced mild heat transfer deterioration ($E_{1e} = 0.95$). The cause for this discrepancy cannot be the difference in bar thickness, as this was only about 3%. The main difference between these two grids is that SSG150-B has a vertical bar close to the heated side of the plate (Fig. 2(e)), whereas SSG150 has open space (Fig. 2(d)). Apparently, some heat transfer obstruction mechanism dominated over any enhancement by turbulence in the wake of this bar. This issue will also be revisited in Section 5.

Some interesting observations can be also made while comparing the results for different MIGs. Among these, MIG-I was the one which enhanced most the heat transfer ($E_{1e} = 1.20$),

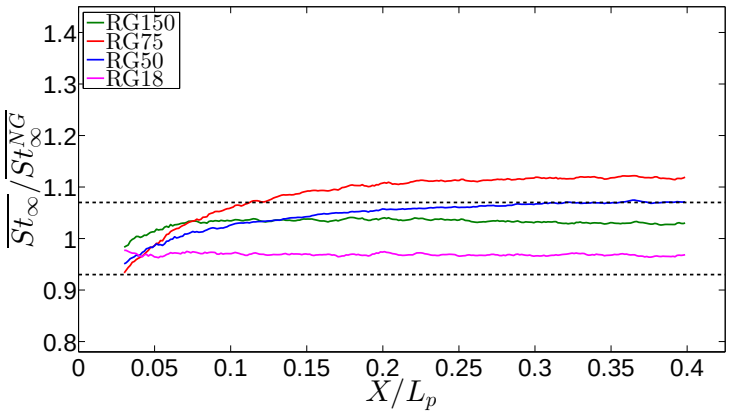

(a) RGs

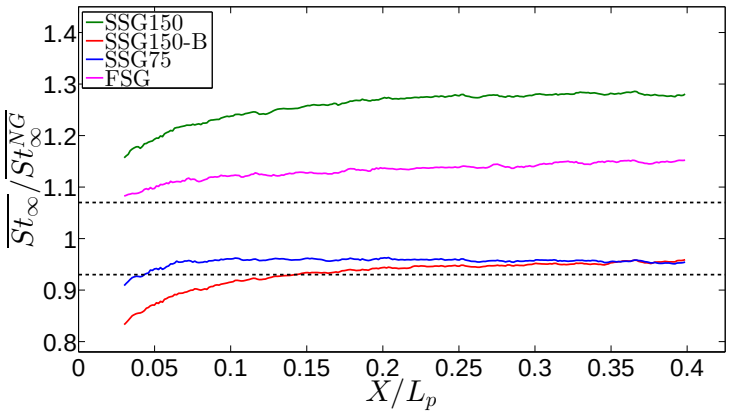

(b) SSGs and FSG

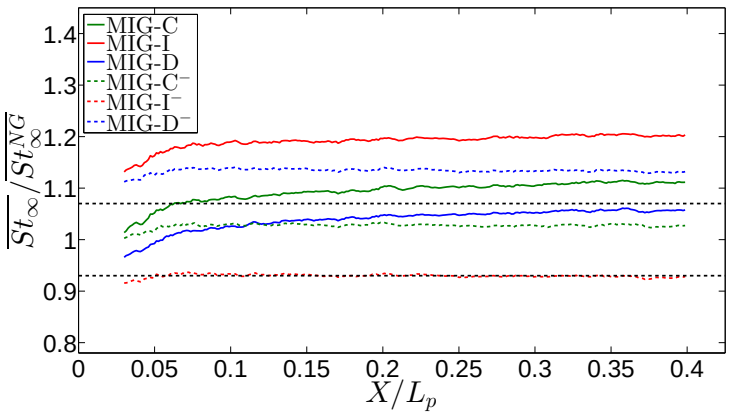

(c) MIGs

Fig. 10: Streamwise variation of the ratio $\overline{St_\infty}/\overline{St_\infty^{NG}}$ on the first portion of the plate (FOV1) for all grids; $x_{LE}/H_t = 1.5$. Black horizontal dashed lines mark the values 0.93 and 1.07.

whereas MIG-I$^-$, namely the same grid as MIG-I but with an inverted orientation, produced stronger heat transfer deterioration ($E_{1e} = 0.93$) than any other grid. Similar differences in heat transfer, although not as prominent, were observed for the pairs MIG-C/MIG-C$^-$ and MIG-D/MIG-D$^-$. In all three cases, stronger heat transfer was produced when the mean shear was

oriented such that the high-velocity side was towards the plate. The stronger the shear was, the stronger the effect of grid inversion would be. Besides affecting the mean velocity field, the geometry and orientation of each grid also affected the turbulence, which could in turn affect heat transfer. One may assert, however, that grid-turbulence effects did not dominate heat transfer in the present configurations by noting that inversion of all three grids produced weaker near-wall turbulence, whereas the heat transfer rate was reduced for MIG-I and MIG-C but increased for MIG-D. This issue will be discussed further in Section 5.

4.4 Heat transfer enhancement produced by the best performing grids

IR measurements in FOV2 ($0.45 \leq X/L_p \leq 0.85$) for $x_{LE}/H_t = 1.5$ were further performed for the five grids that were most effective in enhancing heat transfer in FOV1 ($0.03 \leq X/L_p \leq 0.4$), namely, RG75, SSG150, FSG, MIG-I and MIG-D$^-$. The purpose of these measurements was to confirm that, for these configurations, the heat transfer enhancement persisted on the entire extent of the flat plate. Additionally, IR measurements in FOV2 were performed for SSG150-B to help explain the difference between the performance of this grid and the performance of SSG150.

Contour plots of the ratio St_∞/St_∞^{NG}, both in FOV1 and in FOV2, are shown in Figs. 11 and 12 for the selected configurations. The observation of a smaller spanwise non-uniformity of the ratio St_∞/St_∞^{NG} in FOV2 than in FOV1 can be attributed to the decreasing turbulence inhomogeneity along y downstream of the grids. Stripes of lower heat transfer, separated by stripes of higher heat transfer, can be observed behind bars for RG75, FSG and MIG-I. The contrast between lighter and darker stripes was stronger for MIG-I than for MIG-D$^-$, in consistency with a presumable stronger turbulence inhomogeneity behind MIG-I, which had a longer wake-interaction length scale than MIG-D$^-$ (Valente and Vassilicos, 2014; Melina et al., 2016) for the layers of bars close to the plate (negative z).

The spanwise ($-0.2 \leq Y/H_p \leq 0.2$) averaged heat transfer enhancement parameter $\overline{St_\infty}/\overline{St_\infty^{NG}}$ is shown in Fig. 13(a) for the six selected configurations in both FOV1 and FOV2 with the plate at $x_{LE}/H_t = 1.5$. For all five grids that enhanced heat transfer, the ratio $\overline{St_\infty}/\overline{St_\infty^{NG}}$ in FOV2 deviated by no more than 2.5% from E_{1e} (see Table 4), which means that heat transfer enhancement persisted equally all along the plate. For SSG150-B, $\overline{St_\infty}/\overline{St_\infty^{NG}}$ increased along X in FOV2 but remained lower than 1.05, thus confirming that this grid did not produce an appreciable augmentation of the heat transfer with respect to the NG case.

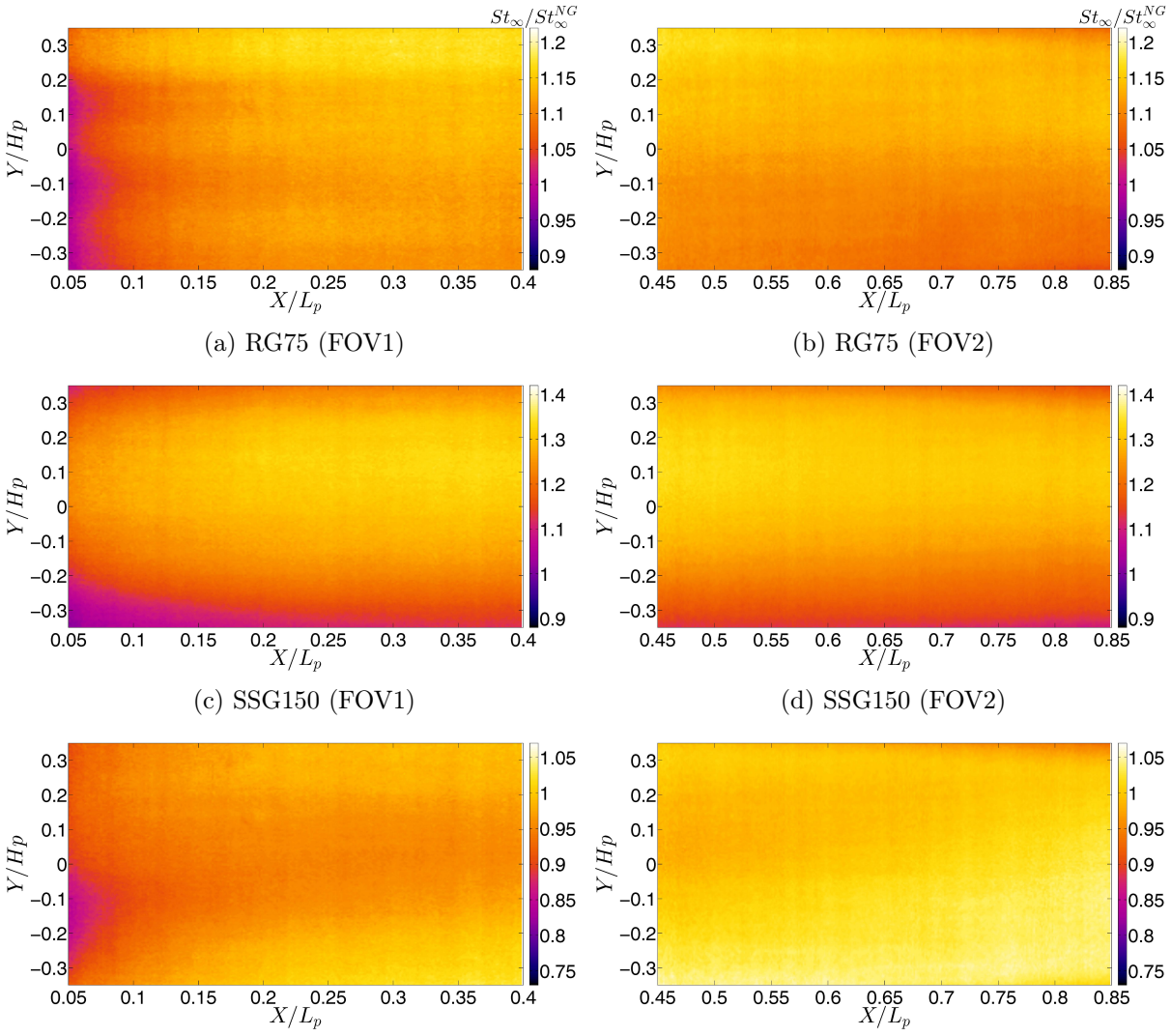

(a) RG75 (FOV1)

(b) RG75 (FOV2)

(c) SSG150 (FOV1)

(d) SSG150 (FOV2)

(e) SSG150-B (FOV1)

(f) SSG150-B (FOV2)

Fig. 11: Contour plots of St_∞/St_∞^{NG} on the plate for RG75 (first row), SSG150 (second row) and SSG150-B (third row); $x_{LE}/H_t = 1.5$. The colour scales vary for different configurations.

For the best performing configurations (RG75, SSG150, FSG, MIG-I and MIG-D$^-$), heat transfer measurements on FOV1 and on FOV2 were also collected with the grids placed at a longer distance from the plate ($x_{LE}/H_t = 5$). The evolution of $\overline{St_\infty}/\overline{St_\infty^{NG}}$ for this set of measurements is shown in Fig. 13(b). As a measure of the overall heat transfer performance of each grid at each position, we used the parameter $E_{1e,2} = (E_{1e} + E_2)/2$, with E_2 defined as the average value of $\overline{St_\infty}/\overline{St_\infty^{NG}}$ in FOV2. It is noted that the difference between E_2 and E_{1e} never exceeded 2.5%. Table 5 shows that the convective heat transfer consistently diminished when the plate was positioned at a longer streamwise distance from the grid where the turbulence intensity was lower. Among the five grids, MIG-I was the only one producing an appreciable heat transfer enhancement when it was placed at $x_{LE}/H_t = 5$. This effect is attributed to the

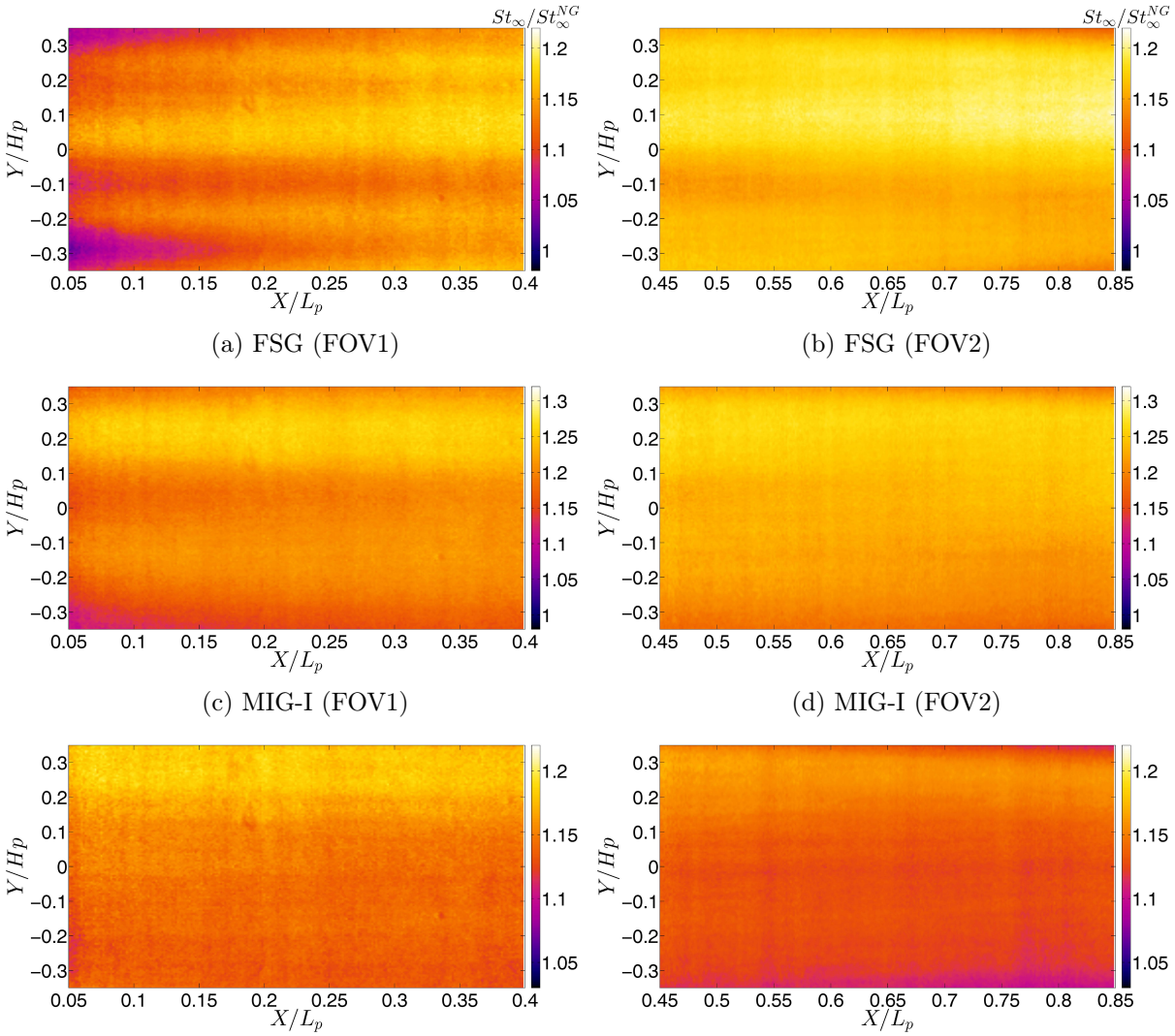

(a) FSG (FOV1)

(b) FSG (FOV2)

(c) MIG-I (FOV1)

(d) MIG-I (FOV2)

(e) MIG-D$^-$ (FOV1)

(f) MIG-D$^-$ (FOV2)

Fig. 12: Contour plots of St_∞/St_∞^{NG} on the plate for FSG (first row), MIG-I (second row) and MIG-D$^-$ (third row); $x_{LE}/H_t = 1.5$. Note that the colour scale is different for each configuration.

Grid	$E_{1e,2}$ $(x_{LE}/H_t = 1.5)$	$E_{1e,2}$ $(x_{LE}/H_t = 5)$
RG75	1.12	1.01
SSG150	1.28	1.05
FSG	1.16	1.04
MIG-I	1.21	1.12
MIG-D$^-$	1.13	1.06

Table 5: Values of $E_{1e,2}$ for the best performing configurations with the grids placed at $x_{LE}/H_t = 1.5$ (slot D) and at $x_{LE}/H_t = 5$ (slot C).

streamwise persistence of higher near–wall velocity caused by this grid.

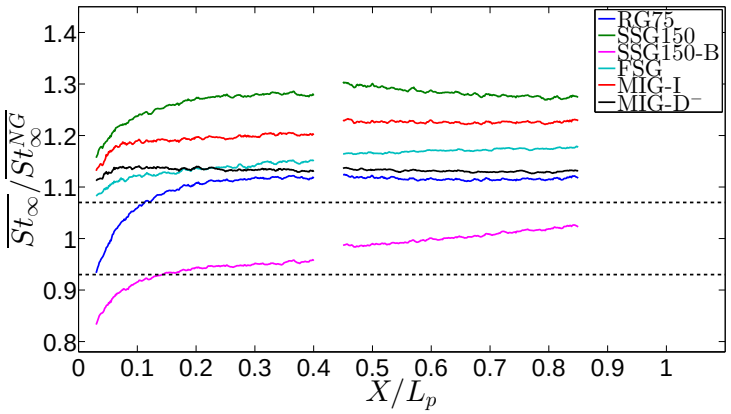

(a) $x_{LE}/H_t = 1.5$

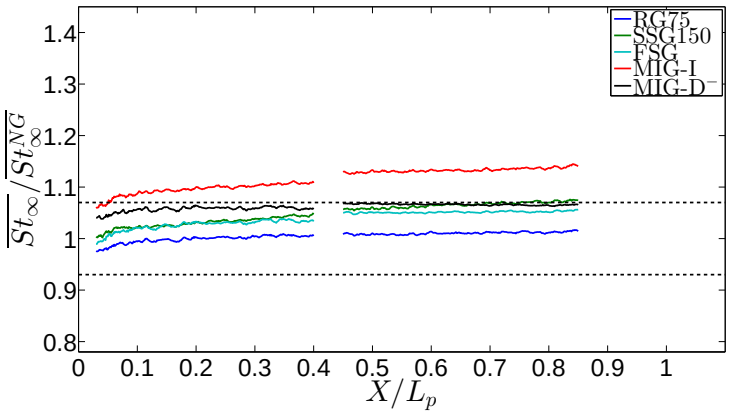

(b) $x_{LE}/H_t = 5$

Fig. 13: Streamwise variation of the ratio $\overline{St_\infty}/\overline{St_\infty^{NG}}$ for selected grids for $x_{LE}/H_t = 1.5$ (a) and 5 (b). Black horizontal dashed lines mark the values 0.93 and 1.07.

5 Correlation between heat transfer and free stream properties

The main objective of this section is to devise a possible correlation of the heat transfer rate with the mean flow profile and the properties of the turbulence produced by the grids used in our experiments. For this purpose, we performed cross-wire measurements with the unheated plate in the wind tunnel and each of the six selected grids RG75, SSG150, SSG150-B, FSG, MIG-I and MIG-D$^-$ positioned so that $x_{LE}/H_t = 1.5$. Measurements were carried out at two downstream stations, $X/L_p = 0.03$ ($x/H_t = 1.8$) and $X/L_p = 0.52$ ($x/H_t = 3.3$), in approximately the half of the test section that contained the plate ($-0.39 \lesssim z/W_t \lesssim 0.06$), and up to a distance of about 10 mm from the plate. Fig. 14 shows the transverse profiles of mean velocity, turbulence intensity, integral length scale and large-scale anisotropy factor u'/w' at the two stations. At $X/L_p = 0.03$, the mean velocity was strongly non-uniform in z for the grids with the largest x^* (SSG150, SSG150-B and FSG). At $X/L_p = 0.52$, all profiles had a reduced non-uniformity,

but those of SSG150-B and the two MIGs maintained significant gradients. It is important to note that, at both stations, U/U_∞ was considerably larger for SSG150 than for SSG150-B in the proximity of the flat plate. The anisotropy ratio u'/w' was approximately constant away from the plate ($-0.2 \leq z/W_t$) and increased steeply with proximity to the wall, in conformity with literature on turbulent boundary layers.

Considering that the turbulence intensity in the present flows is fairly small when compared to 1, we may plausibly assume that there is an approximately linear relationship between the local value of the ratio St_∞/St_∞^{NG} (see Eq. 8) and the turbulence intensity at a reference position z_r, which is outside the boundary layer but close enough to the wall for the flow there to be equivalent to a free stream in uniform flow over a flat plate:

$$\frac{St_\infty}{St_\infty^{NG}} = \frac{U_r}{U_\infty}\left(a + b\,\frac{u'_r}{U_r}\right), \tag{9}$$

where a and b are empirical coefficients. Introducing a "free stream" Stanton number as

$$St_r = \frac{h}{\rho_{film} c_{p_{film}} U_r}, \tag{10}$$

we may write Eq. 9 as

$$\frac{St_r}{St_\infty^{NG}} = a + b\,\frac{u'_r}{U_r}. \tag{11}$$

Before proceeding with the analysis, it is necessary to determine a suitable "free stream" location z_r for each streamwise station for which we had measurements of both the heat transfer rate and flow statistics, namely, for $X/L_p = 0.03$ ($x/H_t = 1.8$) and $X/L_p = 0.52$ ($x/H_t = 3.3$). This task was complicated by the absence of flow measurements within the boundary layer and the general turbulence inhomogeneity. We determined z_r as the location of optimal fit of Eq. 11 to the available results. Fig. 15 shows the sum of squared residuals $res = \sum_{i=1}^{n_o} (\mathcal{D}_i - \mathcal{F}_i)^2$ and the coefficient of determination $R^2 = 1 - res/\left[\sum_{i=1}^{n_o} \left(\mathcal{D}_i - n_o^{-1} \sum_{i=1}^{n_o} \mathcal{D}_i\right)^2\right]$, where $\mathcal{D}_i$ are the measured values of St_r/St_∞^{NG}, $\mathcal{F}_i$ are the predictions of Eq. 11, and $n_o = 6$ is the number of considered grids. An "optimal" $z_r = -0.36W_t$, corresponding to a distance of 27 mm from the plate, was defined confidently for $X/L_p = 0.52$; at that location, res had a clear minimum, while also R^2 had a high maximum (0.91). One may note that $z_r = -0.36W_t$ is also the location where the anisotropy parameter u'/w' began to deviate significantly (by approximately 10%) from its level away from the plate (see Fig. 14(h)). In absence of boundary layer profiles, one

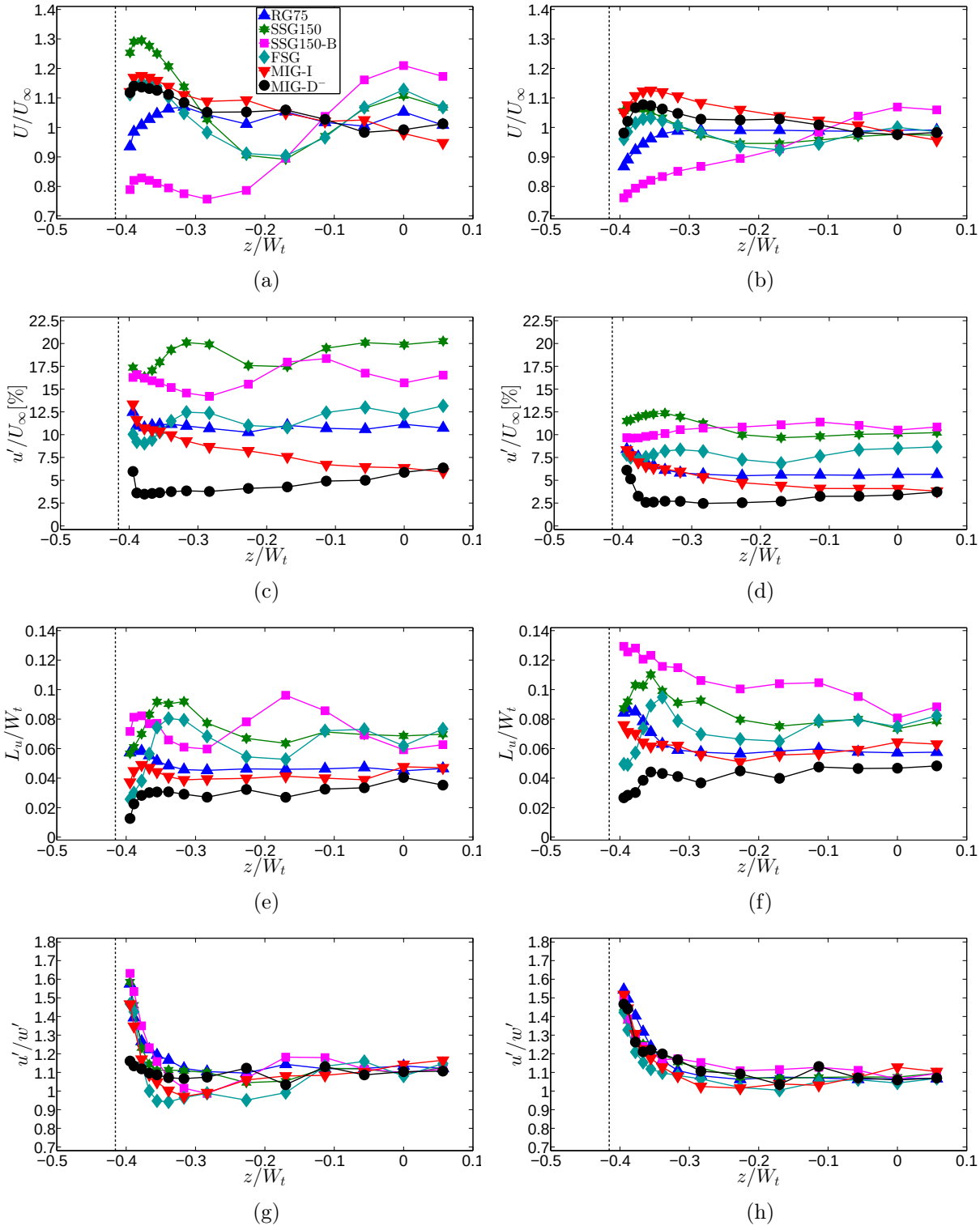

Fig. 14: Transverse (normal to the plate) profiles of mean velocity (first row), turbulence intensity (second row), integral length scale (third row) and large-scale anisotropy factor (fourth row) at $X/L_p = 0.03$ (left column) and $X/L_p = 0.52$ (right column). Vertical dashed lines mark the position ($z/W_t = -0.42$) of the side of the flat plate where the heat transfer was measured.

can therefore use the ratio u'/w' as an indicator of proximity to the plate, and predict the heat transfer coefficient by evaluating the flow properties at the location where this ratio starts to

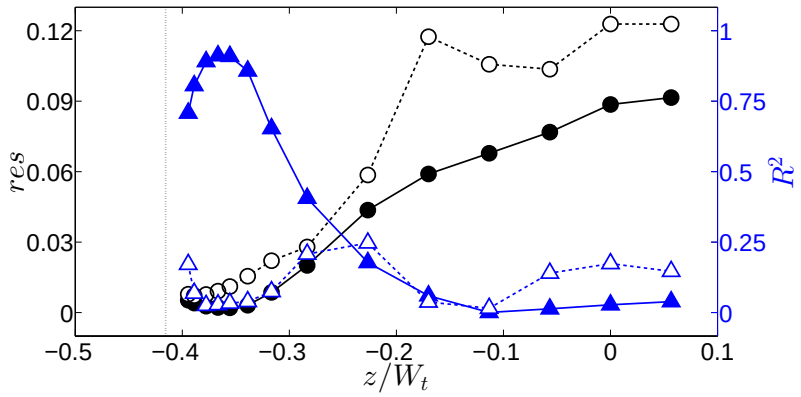

Fig. 15: Sum of squared residuals (black colour) and coefficient of determination (blue colour) of the fit of Eq. 11 to the experimental data at $X/L_p = 0.03$ (empty symbols, dashed lines) and at $X/L_p = 0.52$ (filled symbols, solid lines). The vertical dotted line marks the wall position ($z/W_t = -0.42$).

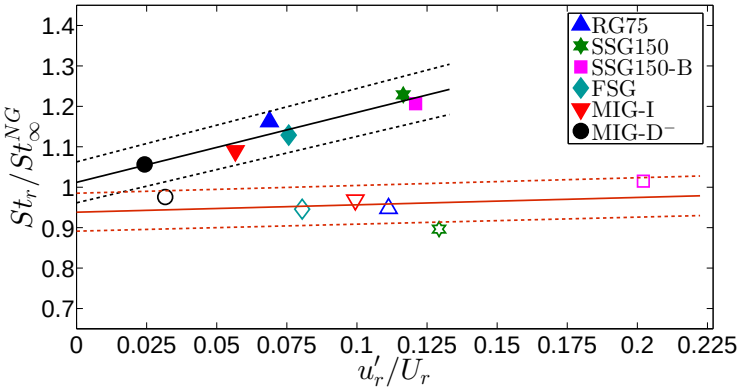

Fig. 16: Heat transfer enhancement against turbulence intensity at $z_r/W_t = -0.39$, $X/L_p = 0.03$ (empty symbols) and at $z_r/W_t = -0.36$, $X/L_p = 0.52$ (filled symbols). The solid lines are linear fits (Eq. 11) to the experimental data and dashed lines mark ±5% deviations from the fits.

increase with respect to its plateau value. For $X/L_p = 0.03$, a weak minimum of res occurred at $z_r = -0.39W_t$ (a distance of 12 mm from the plate), but R^2 was very small for the entire range of z considered.

The ratio St_r/St_∞^{NG} at z_r is plotted against u_r'/U_r in Fig. 16. Near the start of the plate ($X/L_p = 0.03$), this ratio was insensitive to u_r'/U_r, which indicates that the effect of the nearby boundary layer trip and that of free stream mean velocity dominated the local heat transfer and obscured any possible free stream turbulence effect. This explains why R^2 had a small value for the fit of the data at $X/L_p = 0.03$. On the opposite side, at the downstream station $X/L_p = 0.52$ the effect of u_r'/U_r was significant. This is demonstrated by the rise in the value of the coefficient b in Eq. 11 from 0.002 at $X/L_p = 0.03$ to 0.017 at $X/L_p = 0.52$. For $X/L_p = 0.52$ the value of

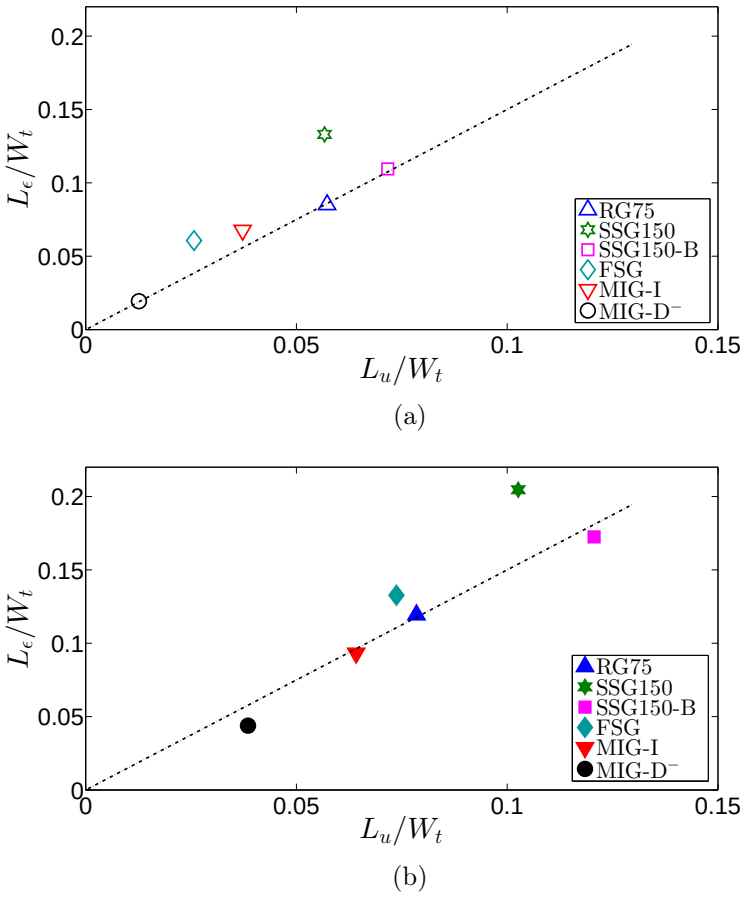

Fig. 17: Values of integral length scale L_u and dissipation length scale L_ϵ at $X/L_p = 0.03$, $z_r/W_t = -0.39$ (a) and $X/L_p = 0.52$, $z_r/W_t = -0.36$ (b). The dot-dashed lines indicate $L_\epsilon = 1.5\,L_u$ ($C_\epsilon = 1$).

the fitted origin a of Eq. 11 was remarkably close to 1 ($a = 1.01$), thus allowing one to recover $St_r \approx St_\infty^{NG}$ in no–grid flow. The observation that the free stream turbulence intensities were approximately the same for grids SSG150 and SSG150-B shows that the difference in heat transfer rates for these two grids was entirely due to differences in free stream velocities. The mean shear rates produced by the present MIGs were too small to allow determination of any mean shear effect, but it seems clear that a grid that generates a sustainable high velocity near the grid (like MIG-I) would enhance heat transfer, despite the decay of turbulence with downstream distance from the grid.

Besides the effect of turbulence intensity, we investigated the possible effect of the length scale of the energy containing motions in the free stream. We considered measurements of the integral length scale L_u as well as estimates of the dissipation length scale $L_\epsilon = 1.5\,u'^3/\epsilon$, computed from measurements of u' and the kinetic energy dissipation rate ϵ. Considering that $L_\epsilon = 1.5 L_u/C_\epsilon$, where the dissipation coefficient is defined as $C_\epsilon = \epsilon L_u/u'^3$, the two length scales would be

proportional to each other only if C_ϵ were constant (see Vassilicos, 2015, for a review on the topic). Figure 17 shows the values of both L_u and L_ϵ at $z = z_r$ for $X/L_p = 0.03$ (Fig. 17(a)) and $X/L_p = 0.52$ (Fig. 17(b)). Despite a considerable variation in the values of L_u and L_ϵ produced by the six selected grids (the largest value of L_ϵ was approximately four times the smallest one for $X/L_p = 0.52$), the ratio St_r/St_∞^{NG} was not correlated with either length scale, after the effect of turbulence intensity was accounted for. In conclusion, for the grids and experimental conditions of the present work, the length scale of the energy containing motions did not have a measurable effect on the heat transfer enhancement by turbulence.

6 Conclusions

Eleven turbulence-generating grids were investigated for their potential to increase the convective heat transfer on a flat plate mounted in a wind tunnel and heated by Joule's effect. The flow downstream of the grids was characterised with hot-wire (cross-wire) measurements, both with and without the flat plate in the wind tunnel. Two-dimensional maps of the local heat transfer coefficient were obtained by measuring the wall temperature distribution on the heated side of the plate with an IR camera. All grids had approximately the same blockage ratio ($\sigma_g = 25\% - 28\%$) and were grouped into three classes: regular square-mesh grids (RGs), single-square grids (SSGs) and multi-scale grids (FSG and MIGs). The three MIGs were designed following the original work of Zheng et al. (2018), and produced shear flows in which the mean velocity was approximately linear in the direction z normal to the plate.

In an effort to assist the design of efficient heat transfer systems, we quantified the heat transfer enhancement produced by each grid and compared results at the same position X on the plate. We found that a substantial enhancement (with respect to the no grid case) in the spanwise-averaged values of the Stanton number can be achieved with SSG150 (by approximately 30%) and with MIG-I (by roughly 20%) when the plate is at a short distance ($x_{LE}/H_t = 1.5$) from the grids. Grid SSG150-B, similar to SSG150 but with a vertical bar close to the heated side of the plate, failed to increase the net heat transfer rate for the same U_∞. For an increased separation between the plate and the grid ($x_{LE}/H_t = 5$), MIG-I was found to be the only grid causing an appreciable increase in the Stanton number (about 10%) that far downstream. For each of the MIGs tested here, the heat transfer behaviour on the plate was found to be very sensitive to the orientation of the grid with respect to the plate, *i.e.* with the larger (MIG-C,

MIG-I and MIG-D) or with the smaller (MIG-C$^-$, MIG-I$^-$ and MIG-D$^-$) multi-scale iterations located close to the heated wall.

Velocity profiles in the direction z normal to the plate were taken for a selected number of grids (RG75, SSG150, SSG150-B, FSG, MIG-I and MIG-D$^-$) in order to explain the heat transfer results. These measurements, taken with the unheated plate in the wind tunnel, showed noticeable non-uniformity of the mean velocity and inhomogeneity of the turbulence at downstream distances that would be along the plate, when it was inserted in the test section. The ratio St_∞/St_∞^{NG} at the mid-length of the plate ($X/L_p = 0.52$) was found to increase with mean velocity and turbulence intensity at a reference downstream distance z_r, which was outside the boundary layer but close enough to the wall for the flow there to be equivalent to a free stream in uniform flow over a flat plate. The location z_r can be approximately predicted as the location where the ratio u'/w' starts to increase with respect to its plateau value (away from the plate). In the proximity of the step used to promote transition, the ratio St_∞/St_∞^{NG} was found to increase with mean velocity but also to be insensitive to the turbulence intensity in the range $3\% < u'/U < 20\%$. It is speculated that the heat transfer behaviour at the beginning of the plate was dominated by tripping effects rather than by free stream turbulence. Differently from other empirical studies (see e.g. Hancock and Bradshaw, 1983; Blair, 1983) on heat transfer enhancement from a flat plate, neither the integral length scale L_u nor the dissipation length scale L_ϵ were found to significantly affect the heat transfer augmentation for the range of experimental conditions tested here. A full resolution of this contradiction is left for future works where: (i) dedicated boundary layer measurements could be performed, (ii) a larger range of integral/dissipation length scales could be produced, and (iii) several relative grid-plate positions could be tested.

From a practical point of view, this work showed that, for the operating conditions of this experiment and for a value of $\sigma_g = 28\%$: (i) single-square grids (SSGs) with large t_0/L_0 and large x^* are a simple and effective solution to increase the heat transfer on a flat plate close to the grid; (ii) the bars of the SSGs should be placed sufficiently far from the heated wall (SSG150), so that they would not introduce a strong mean velocity deficit near the wall (SSG150-B), which can prevent a net heat transfer augmentation despite high local turbulence levels; (iii) multi-scale inhomogeneous grids (MIGs), which generate turbulent shear flows, are effective in enhancing heat transfer, even with large separation between the grid and the plate ($x_{LE}/H_t = 5$), and their design can be optimised to produce high values of both mean velocity and turbulence intensity

close to the wall; (iv) the most efficient configuration for the MIGs tested here is that of MIG-I for which the multi-scale iterations with lower blockage and thicker bars are on the same side of the plate.

It is important to stress that the mean shear rate produced by the MIGs tested here was too low to assess its role on the convective heat transfer from a flat plate. New dedicated experiments with grids and/or other shear flows generators should be carried out to shed light on this issue, i.e. to investigate the effect of the mean velocity gradient as decoupled to that of mean velocity and turbulence intensity. Here it has been shown that MIGs can be used to produce mean velocity profiles which are linear in the transverse direction, and therefore invariant with downstream distance x from the grid for some appreciable range of x. As a result, producing a turbulent shear flow with the MIGs is an efficient solution to achieve sustained heat transfer enhancement over long distances, in contrast to all other types of grids tested here.

Acknowledgements

G.M., P.J.K.B. and J.C.V. acknowledge support from the EU through the FP7 Marie Curie MULTISOLVE project (Grant No. 317269). J.C.V. also acknowledges the support of an ERC Advanced Grant (Grant No. 320560).

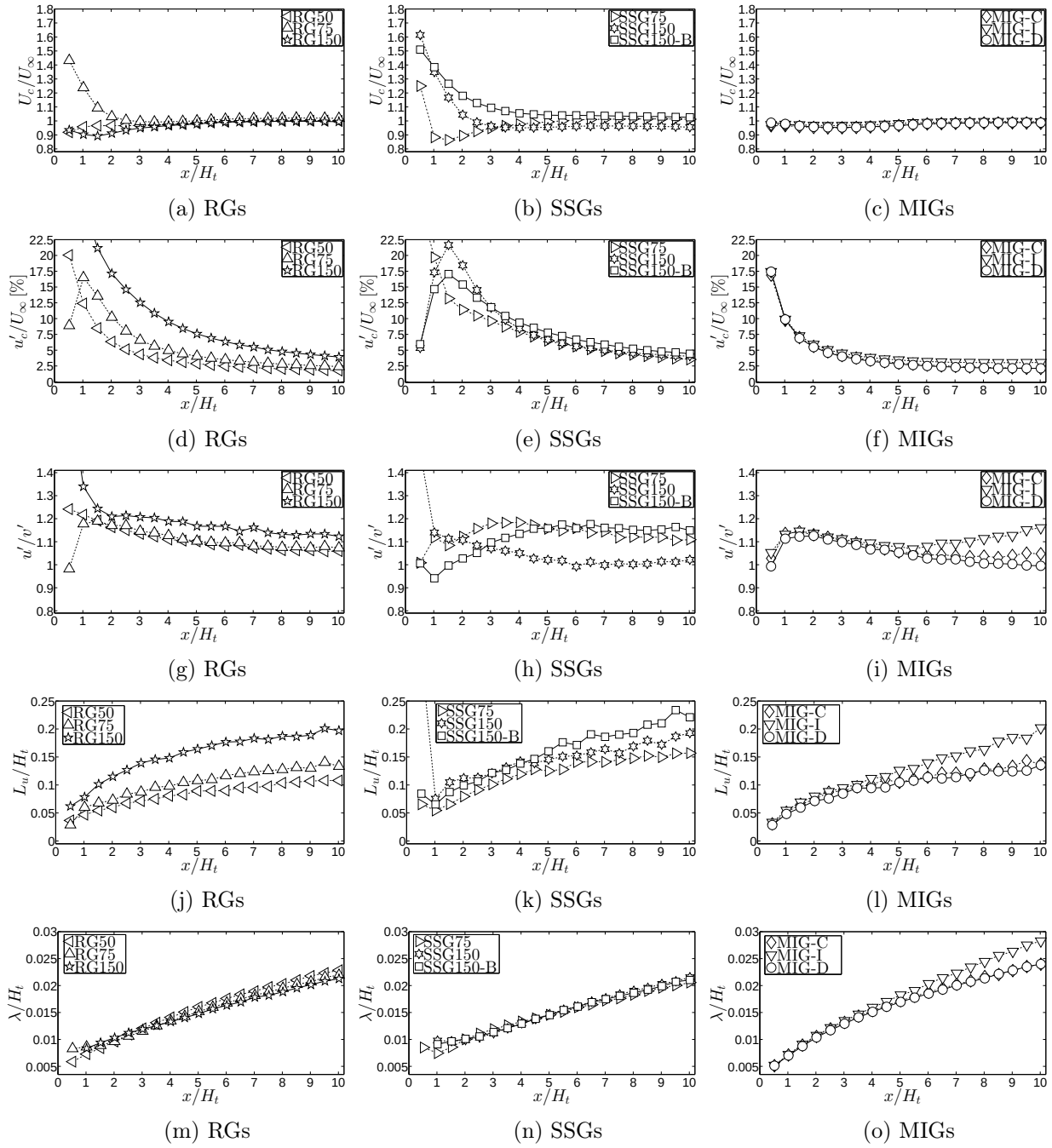

(a) RGs (b) SSGs (c) MIGs

(d) RGs (e) SSGs (f) MIGs

(g) RGs (h) SSGs (i) MIGs

(j) RGs (k) SSGs (l) MIGs

(m) RGs (n) SSGs (o) MIGs

Fig. 18: Centreline mean velocity (first row), turbulence intensity (second row), large-scale anisotropy factor (third row), integral length scale (fourth row) and Taylor length scale (fifth row) for RGs (first column), SSGs (second column) and MIGs (third column).

Appendix: Centreline turbulence statistics

The centreline mean velocity U_c for the three categories of grids (RGs, SSGs and MIGs) is shown in Figs. 18(a)-(c). For configurations for which the centreline passes through an open section of the grid (RG75 and SSGs, see Fig. 2), rather than through a bar, U_c/U_∞ was sensibly larger than 1 in the proximity of the grid ($x/H_t \lesssim 1$) and then decreased downstream. This is consistent

with the presence of a jet at each opening of the grid and a wake behind each bar, which resulted in a pronounced inhomogeneity of the flow in the very near-field of the grid. The streamwise evolution of the centreline turbulence intensity is shown in Figs. 18(d)-(f) and is discussed in Section 3.1 of this paper.

The large-scale anisotropy factor u'/v' is shown in Figs. 18(g)-(i) for the various grids. Following a near-field developing region, the ratio u'/v' approached a constant value close to 1 for almost all configurations, thus indicating that the centreline large-scale turbulent fluctuations became isotropic at a sufficient distance from the grid. For MIG-I the ratio u'/v' increased with x for $x/H_t \gtrsim 5.5$ (see Fig. 18(i)) in contrast to the other configurations. Figs. 18(j)-(l) and Figs. 18(m)-(o) show respectively the integral length scale L_u and the Taylor length scale λ. Both L_u and λ increased with x but, while L_u also increased with the distance between the bars L_0, λ was found to be on the contrary almost invariant with L_0. Note in fact that the centreline profiles of λ are approximately collapsed for the RGs (Fig. 18(m)) and for the SSGs (Fig. 18(n)). One can see that both L_u and λ increased faster with x for MIG-I than for MIG-C and MIG-D when $x/H_t \gtrsim 5.5$, this being also the location where the ratio u'/v' started to increase for MIG-I. Since the MIGs shared a very similar geometry and considering that the magnitude of the shear rate was the highest for MIG-I (see Section 3.2), it is possible that the higher shear was the cause for the higher growth of the turbulence length scales.

For the two grids with the highest values of t_0, SSG150 and SSG-150B, one can expect the vortex shedding from their bars to be clearly detectable, at least close to the grid. For this purpose, the power spectral densities of u and v, E_u and E_v, are shown in Figs. 19(a)-(b) for SSG150 and in Figs. 19(c)-(d) for SSG150-B (sketches of the two grids are also shown in the same figures) at a series of downstream locations. For both grids, the energy spectra exhibit a well-defined inertial range where $E_u \propto f^{-p_u}$ and $E_v \propto f^{-p_v}$, with p_u and p_v both close to 5/3. For the positions closer to the grids ($x/x_{peak} \leq 1$) it is possible to distinguish a dominant frequency f_{sh} where the energy spectra show a clear peak, i.e. the vortex shedding frequency of the bars. This frequency was $f_{sh}t_0/U_\infty = 0.21$ for both SSG150 and for SSG150-B. It is interesting to note that, differently from SSG150, for SSG-150-B the spectrum of u (see Figs. 19(c)) shows a second clear peak at a higher frequency, $ft_0/U_\infty = 0.33$. Since this second peak is not present in the energy spectrum of v (see Figs. 19(d)), it perhaps appears as a result of the interaction between the shedding motions from the vertical bars (separated by a distance of $L_0/2$) of SSG150-B (see Fig. 2(e)).

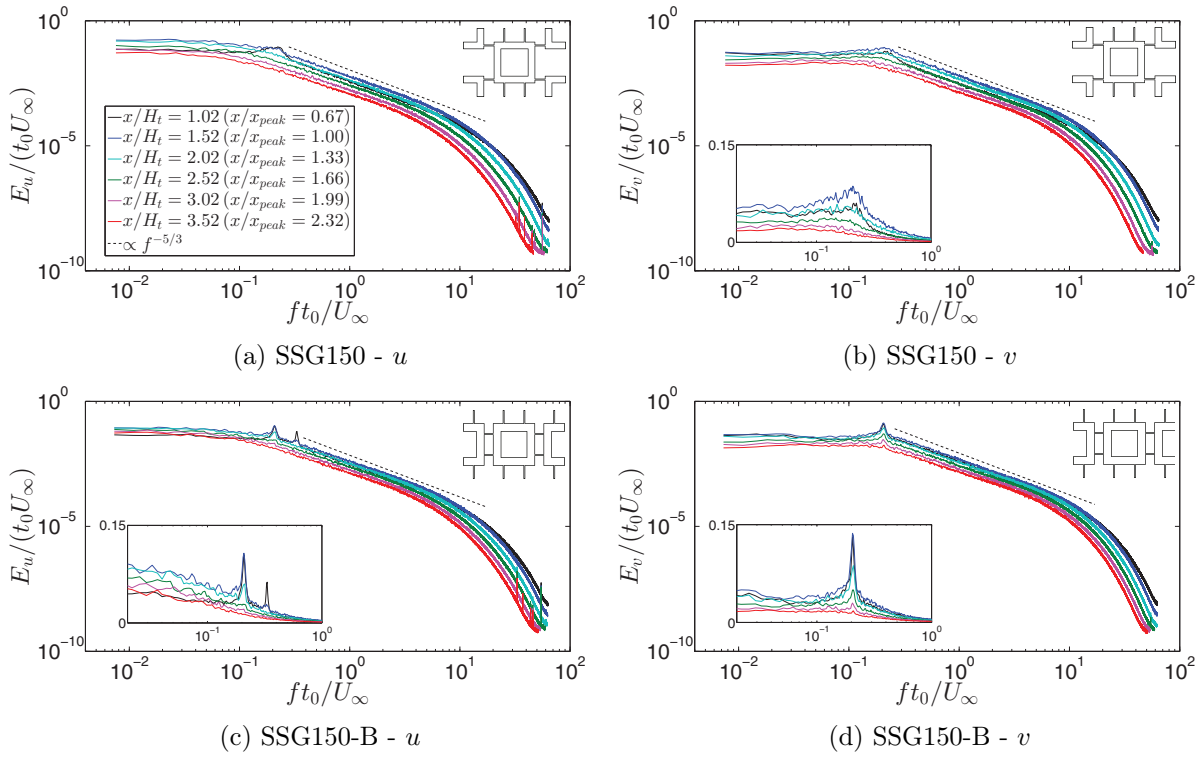

(a) SSG150 - u (b) SSG150 - v

(c) SSG150-B - u (d) SSG150-B - v

Fig. 19: Power spectral density of u (left) and of v (right) on the centreline for SSG150 (top) and SSG150-B (bottom).

References

Blair, M. F. (1983). Influence of free-stream turbulence on turbulent boundary layer heat transfer and mean profile development, Part II - Analysis of results. *J. Heat Trans.-T. ASME*, 105:41–47.

Cafiero, G., Castrillo, G., Greco, C. S., and Astarita, T. (2017). Effect of the grid geometry on the convective heat transfer of impinging jets. *Int. J. Heat Mass Transfer*, 104:39–50.

Cafiero, G., Discetti, S., and Astarita, T. (2014). Heat transfer enhancement of impinging jets with fractal-generated turbulence. *Int. J. Heat Mass Transfer*, 75:173–183.

Castro, I. P. (1984). Effects of free stream turbulence on low Reynolds number boundary layers. *J. Fluid. Eng.-T. ASME*, 106:298–306.

Colleoni, A., Toutant, A., Olalde, G., and Foucaut, J. M. (2013). Optimization of winglet vortex generators combined with riblets for wall/fluid heat exchange enhancement. *Appl. Therm. Eng.*, 50:1092–1100.

Daguenet-Frick, X., Toutant, A., Bataille, F., and Olalde, G. (2013). Numerical investigation of a ceramic high-temperature pressurized-air solar receiver. *Sol. Energy*, 90:164–178.

DeGraaff, D. B. and Eaton, J. K. (2000). Reynolds-number scaling of the flat-plate turbulent boundary layer. *J. Fluid Mech.*, 422:319–346.

Dogan, E., Hanson, R. E., and Ganapathisubramani, B. (2016). Interactions of large-scale free-stream turbulence with turbulent boundary layer. *J. Fluid Mech.*, 802:79–107.

Erm, L. P. and Joubert, P. N. (1991). Low-Reynolds-number turbulent boundary layers. *J. Fluid Mech.*, 230:1–44.

Gomes-Fernandes, R., Ganapathisubramani, B., and Vassilicos, J. C. (2012). Particle image velocimetry study of fractal-generated turbulence. *J. Fluid Mech.*, 711:306–336.

Hancock, P. E. and Bradshaw, P. (1983). The effect of free-stream turbulence on turbulent boundary layers. *J. Fluid. Eng.-T. ASME*, 105:284–289.

Hewitt, G. F. (2008). *Heat Exchanger Design Handbook*. Begell House, New York.

Hurst, D. and Vassilicos, J. C. (2007). Scalings and decay of fractal-generated turbulence. *Phys. Fluids*, 19(3):035103.

Junkhan, G. H. and Serovy, G. K. (1967). Effects of free-stream turbulence and pressure gradient on flat-plate boundary-layer velocity profiles and on heat transfer. *J. Heat Trans.-T. ASME*, 89:169–175.

Kestin, J., Maeder, P. F., and Wang, H. E. (1961). Influence of turbulence on the transfer of heat from plates with and without a pressure gradient. *Int. J. Heat Mass Transfer*, 3:133–154.

Laizet, S., Nedić, J., and Vassilicos, J. C. (2015). The spatial origin of -5/3 spectra in grid-generated turbulence. *Phys. Fluids*, 27:065115.

Laizet, S. and Vassilicos, J. C. (2011). DNS of fractal-generated turbulence. *Flow Turbul. Combust.*, 87:673–705.

Lueptow, R. M., Breuer, K. S., and Haritonidis, J. H. (2004). Computer-aided calibration of X-probes using a look-up table. *Exp. Fluids*, 6:115–118.

Maciejewski, P. K. and Moffat, R. J. (1992). Heat transfer with very high free-stream turbulence: Part II - Analysis of results. *J. Heat Trans.-T. ASME*, 114:834–839.

Mazellier, N. and Vassilicos, J. C. (2010). Turbulence without Richardson-Kolmogorov cascade. *Phys. Fluids*, 22:075101.

McDonald, H. and Kreskovsky, J. P. (1974). Effect of free-stream turbulence on the turbulent boundary layer. *Int. J. Heat Mass Transfer*, 17:705–716.

Melina, G., Bruce, P. J. K., Hewitt, G. F., and Vassilicos, J. C. (2017). Heat transfer in production and decay regions of grid-generated turbulence. *Int. J. Heat Mass Transfer*, 109:537–554.

Melina, G., Bruce, P. J. K., and Vassilicos, J. C. (2016). Vortex shedding effects in grid-generated turbulence. *Phys. Rev. Fluids*, 1:044402.

Moffat, R. J. (1988). Describing the uncertainties in experimental results. *Exp. Therm. Fluid Sci.*, 1:3–17.

Nagata, K., Sakai, Y., Inaba, T., Suzuki, H., Terashima, O., and Suzuki, H. (2013). Turbulence structure and turbulence kinetic energy transport in multiscale/fractal-generated turbulence. *Phys. Fluids*, 25(6):065102.

Nedić, J. and Tavoularis, S. (2016a). Energy dissipation scaling in uniformly sheared turbulence. *Phys. Rev. E*, 93:033115.

Nedić, J. and Tavoularis, S. (2016b). Measurements of passive scalar diffusion downstream of regular and fractal grids. *J. Fluid Mech.*, 800:358–386.

Pohlhausen, E. (1921). Der Warmeaustausch zwischen festen Korpern und Flussigkeiten mit kleiner reibung und kleiner Warmeleitung. *Zamm-Z. Angew. Math. Me.*, 1:115–121.

Pope, S. B. (2000). *Turbulent Flows*. Cambridge University Press, Cambridge.

Rohr, J. J., Itsweire, E. C., Helland, K. N., and Van Atta, C. W. (1988). An investigation of the growth of turbulence in a uniform-mean-shear flow. *J. Fluid Mech.*, 187:1–33.

Sak, C., Liu, R., Ting, D. S., and Rankin, G. W. (2007). The role of turbulence length scale and turbulence intensity on forced convection from a heated horizontal circular cylinder. *Exp. Therm. Fluid Sci.*, 31:279–289.

Schlatter, P. and Örlü, R. (2012). Turbulent boundary layers at moderate Reynolds numbers: infow length and tripping effects. *J. Fluid Mech.*, 710:5–34.

Serra, S., Toutant, A., and Bataille, F. (2012). Thermal large eddy simulation in a very simplified geometry of a solar receiver. *Heat Transfer Eng.*, 33:505–524.

Sharp, N. S., Neuscamman, S., and Warhaft, Z. (2009). Effects of large-scale free stream turbulence on a turbulent boundary layer. *Phys. Fluids*, 21:095105.

Sugawara, S., Sato, T., Komatsu, H., and Osaka, H. (1988). Effect of free-stream turbulence on flat plate heat transfer. *Int. J. Heat Mass Transfer*, 31:5–12.

Tavoularis, S. and Corrsin, S. (1981). Experiments in nearly homogenous turbulent shear flow with a uniform mean temperature gradient. Part 1. *J. Fluid Mech.*, 104:311–347.

Tavoularis, S. and Karnik, U. (1989). Further experiments on the evolution of turbulent stresses and scales in uniformly sheared turbulence. *J. Fluid Mech.*, 204:457–478.

Thole, K. A. and Bogard, D. G. (1995). Enhanced heat transfer and shear stress due to high free-stream turbulence. *J. Turbomach.*, 117:418–424.

Valente, P. C. and Vassilicos, J. C. (2014). The non-equilibrium region of grid-generated decaying turbulence. *J. Fluid Mech.*, 744:5–37.

Vassilicos, J. C. (2015). Dissipation in Turbulent Flows. *Annu. Rev. Fluid Mech.*, 47:95–114.

von Kármán, T. (1939). The analogy between fluid friction and heat transfer. *Trans. ASME*, 61:705–710.

Zheng, S., Bruce, P. J. K., Graham, J. M. R., and Vassilicos, J. C. (2018). Weakly sheared turbulent flows generated my multiscale inhomogeneous grids. *Under consideration for publication in J. Fluid Mech.*